Similar to restin	1.270573974		0.644315183	2.108628035	0.602559626	2.654606104	Cytoplasm	Other
Neuromodulin	1.258924961		0.650084972	2.089296103	0.602559626	2.630268097	Plasma membrane	Other
DnaJ homolog subfamily C member 3	0.794328213		0.667952716	2.089296103	0.376703799	1.659587026	Cytoplasm	Other
Unnamed protein product	0.794328213		0.674318373	2.089296103	0.380189389	1.659587026	Nucleus	Transcription regulator
Hyperosmotic glycine rich protein-like	0.787045777	0.041524451	0.524631321	1.247382998	0.591561615	0.981747925	Nucleus	Other
Unnamed protein product	0.787045777		0.657890975	2.089296103	0.373250186	1.644371986	Cytoplasm	Kinase
Small nuclear ribonucleoprotein-associated protein B	0.779830098		0.650910974	2.089296103	0.373250186	1.629295945	Nucleus	Other
Glyceraldehyde-3-phosphate dehydrogenase	0.765596628		0.629889786	2.089296103	0.366437614	1.599557996	Cytoplasm	Enzyme
4-aminobutyrate aminotransferase, mitochondrial precursor	0.758577585		0.622181296	2.108628035	0.363078088	1.599557996	Cytoplasm	Enzyme
Aldolase a, fructose-bisphosphate 1	0.758577585		0.61985302	2.108628035	0.363078088	1.599557996	Cytoplasm	Enzyme
Unnamed protein product	0.758577585		0.620348215	2.108628035	0.363078088	1.599557996	Cytoplasm	Transporter
Novel protein similar to human general control of amino-acid synthesis 1-like 1	0.751622915		0.608968377	2.089296103	0.359749287	1.570363045	Cytoplasm	Translation regulator
60S ribosomal protein L24	0.731139123		0.58094883	2.108628035	0.349945188	1.541700006	Cytoplasm	Other
Triosephosphate isomerase	0.731139123	0.020682539	0.375185192	1.16949904	0.515228629	0.855066717	Cytoplasm	Enzyme
Proprotein convertase subtilisin/kexin type 1	0.717794299		0.565635085	2.108628035	0.343558013	1.51356101	Extracellular space	Peptidase
Hemoglobin subunit beta	0.711213529		0.548802316	2.089296103	0.337287307	1.485936046	Cytoplasm	Transporter
Prothymosin alpha	0.691830993	0.041728616	0.526520073	1.419057012	0.373250186	0.981747925	Nucleus	Transcription regulator
Unnamed protein product	0.685488224		0.515590072	2.089296103	0.325087309	1.432188034	Cytoplasm	Enzyme
Alpha-globin 4	0.679203629	0.130065185	0.892440081	1.472311974	0.405508488	1	Cytoplasm	Transporter
Hemoglobin subunit beta-1	0.679203629	0.029096079	0.370831192	1.224616051	0.165958703	0.831763685	Cytoplasm	Transporter
Calreticulin	0.660693526	0.087643152	0.574053884	1.584892988	0.187068194	1.047129035	Cytoplasm	Transcription regulator
Unnamed protein product	0.648634374		0.471870601	2.089296103	0.307609707	1.355188966	unknown	Other
SMEK homolog 2	0.625172675		0.450730801	2.108628035	0.299226493	1.318256974	unknown	Other
Unnamed protein product	0.625172675	0.003137056	0.454783201	2.108628035	0.299226493	1.318256974	Cytoplasm	Other
Gonadotrophin alpha 1 subunit	0.625172675	0.035022072	0.778641701	1.29419601	0.291071713	0.809095919	Extracellular space	Other
Follicle stimulating hormone beta subunit	0.619441092	0.045384203	0.358060092	1.380383968	0.383707315	0.855066717	Extracellular space	Other
Hypothetical protein LOC335859	0.586138189		0.409159511	2.108628035	0.280543387	1.235947013	Cytoplasm	Enzyme
Dynactin subunit 2	0.529663384	0.019913448	0.269459903	1.570363045	0.017701089	0.831763685	Cytoplasm	Other
Melanin concentrating hormone 2 (MCH2) precursor	0.510505021	0.189016216	0.694045424	1.940886021	0.27289781	0.990831971	Extracellular space	Other
60S acidic ribosomal protein P2	0.428548515		0.27934891	2.108628035	0.205116197	0.90364939	Cytoplasm	Other
Rho GDP-dissociation inhibitor 1	0.398107201	0.127483736	0.273517191	2.290868044	0.021086279	0.912010789	Cytoplasm	Other
Hypothetical protein LOC569455	0.325087309		0.216371298	2.108628035	0.154170096	0.685488224	Nucleus	Transporter
Growth hormone 2	0.207014099	0.076665109	0.229496703	2.398833036	0.098174803	0.496592313	Extracellular space	Cytokine
Somatolactin (alpha)	0.1458814	0.06390252	6.09E-05	3.311311007	0.046989411	0.48305881		

reagents and MS/MS in the amago salmon pituitary, treated (or not) with excess GH1.

In the iTRAQ-MS/MS analysis, we identified 1178 unique proteins (confidence > 95%) from 26,800 spectra; 569 unique proteins at the 5% FDR threshold level. Additionally, by the statistical analysis performed using the ProteinPilot 3.0 software, we defined 63 unique proteins that exhibited differential expression (≥1.25-fold change) in pituitaries cultured with excess GH1.

In order to understand the function of the differentially expressed proteins, we used the IPA software to classify these proteins according to their subcellular localizations, molecular functions, and biological functions. In this analysis, because the fish protein database is not rich in functional information compared to databases for human and mouse, we used BLAST to cross-reference the differentially expressed proteins with their counterparts in the human non-redundant protein database. Among the 63 unique proteins, 61 were identified as having human homologs.

First, these 61 differentially expressed proteins were classified into five discrete subcellular localization categories (cytoplasm, nucleus, plasma membrane, extracellular space, and other). About half of the differentially expressed proteins (59.0%) are localized to the cytoplasm (Fig. 1A).

Second, we classified the 61 proteins into the following eight categories based on their molecular function: enzyme, transporter, peptidase, transcription regulator, cytokine, kinase, translation regulator, and other. Among the 61 proteins, 52.5% of the differentially expressed proteins were classified into multiple categories; 39.4% were classified in single categories as either enzyme (14.8%), transporter (13.1%), peptidase (6.6%) or transcriptional regulation (4.9%) (Fig. 1B).

Third, we classified the proteins based on their biological function ontology. This analysis revealed that many of the proteins that are differentially expressed in response to excess GH1 treatment are molecules related to endocrine systems, cell growth and proliferation, and metabolism (Fig. 1C).

3.1.1. *Endocrine systems*

Fig. 2 indicates the expression levels of peptide hormones in the excess GH1-treated pituitary. In this study, although the expression of endogenous GH1 did not change in response to excess GH1 treatment, levels of the paralogous GH2 decreased; those data suggest that GH2 expression in the amago salmon pituitary is suppressed by excess GH1 treatment.

Another pituitary hormone, somatolactin (SL), which belongs to the GH/PRL family, has been identified only in fishes. SL has two isoforms (SLA and SLB), which are expressed in different sites within the pituitary [28]. Although SL plays important roles in growth, reproduction and metabolism, the functional difference (if any) between SLA and SLB remains unclear. In the proteome analysis, the expression level of SLA, but not SLB, decreased markedly in the GH1-treated pituitary; those data suggest that the two isoforms of SL might be differently regulated by excess GH1 treatment, just as GH1 and GH2 are. However, it is still not clear how differences in expression levels among isoforms of GH and SL affect physiological functions in salmon.

In contrast, two isoforms (PRL1 and PRL2) of PRL, a peptide hormone belonging to GH family, were increased in the excess GH1-treated pituitary (Fig. 2). PRL stimulates increases in food intake and body weight [4]. PRL2 is expressed only in fish, and its function has been postulated to be similar to that of PRL [29]. Up-regulation of both PRL1 and PRL2 in the pituitary in response to excess GH1 treatment might be involved in enhancement of food intake and increase of body weight.

Proteome analysis indicated that glycoprotein hormone FSH, consisting of an α-subunit (CGA) and β-subunit (FSHB), was also decreased in the excess GH1-treated pituitary (Fig. 2). FSH is a major regulator of gonadal development, and is required for oogenesis in females and spermatogenesis in males. Further, inhibition of the FSH receptor induces abnormalities in ovogenesis and spermatogenesis in salmon [6]. Thus, the down-regulation of FSH in the pituitary by excess GH1 treatment might induce attenuation of gonadal development and abnormal fertility. Furthermore, CGA is a subunit of another pituitary glycoprotein hormone, TSH and LH, whose β-subunits are TSHB and LHB, respectively [1,2]. Therefore, down-regulation of CGA by excess GH1 treatment might affect formation and functions of TSH and LH even though levels of LHB and TSHB do not change.

The expression levels of proteins related to hormone production of pituitary also changed in response to excess GH1 treatment (Table 2). PHD finger protein 17 (PHF17) is an E3 ubiquitin ligase that targets β-catenin for proteasomal degradation [30]. β-Catenin is a major component of cell–cell adherence junctions; in the pituitary, it plays a role in cellular organization and cell–cell signaling, which are important for production and secretion of pituitary hormone [31]. Therefore, in the excess GH1-treated pituitary, up-regulation of PHF17 might influence production and secretion of pituitary hormone via the disruption of the pituitary cell network, mediated by downregulation of β-catenin.

Calcium/calmodulin-dependent protein kinase II γ (CAMK2G) is one component of calcium/calmodulin-dependent kinase II (Ca/CAMK II), and plays a key role as a calcium signaling mediator in various tissues, including the pituitary. In the pituitary, Ca/CAMK II increases the mRNA expression level of some pituitary hormones [32,33]. Thus, down-regulation of CAMK2G would presumably affect the expression levels of these hormones (Table 2). Proprotein convertase subtilisin/kexin type 1 (PCSK1), which is expressed in brain and endocrine organs including pituitary, plays a major role in proteolytic cleavage of peptide hormones (e.g., POMC) and neuropeptide precursors. PCSK1 null mice and humans with loss-of-function PCSK1 mutations exhibit multiple endocrine defects [34,35]. Thus, in the excess GH1-treated pituitary, down-regulation of PCSK1 might lead to multiple endocrine defects as a result of impaired hormone processing (Table 2).

Taken together, the balance and regulation of various hormones in the pituitary were influenced by excess GH1 treatment. The induced imbalance of pituitary hormones might affect the regulation of many biological and physiological functions in excess GH1-treated salmon.

3.1.2. *Cell growth and cell proliferation*

In our proteome analysis, we investigated differential expression dynamics of proteins, including metabolic enzymes, ribosomal proteins, and proliferation related proteins, in the excess GH1-treated pituitary. Aldolase C (ALDOC), triosephosphate isomerase 1 (TPI1), and glyceraldehyde-3-phosphate dehydrogenase (GAPDH) are enzymes of the glycolytic pathway, involved in the conversion of glucose into lactate or pyruvate. Mitochondrial

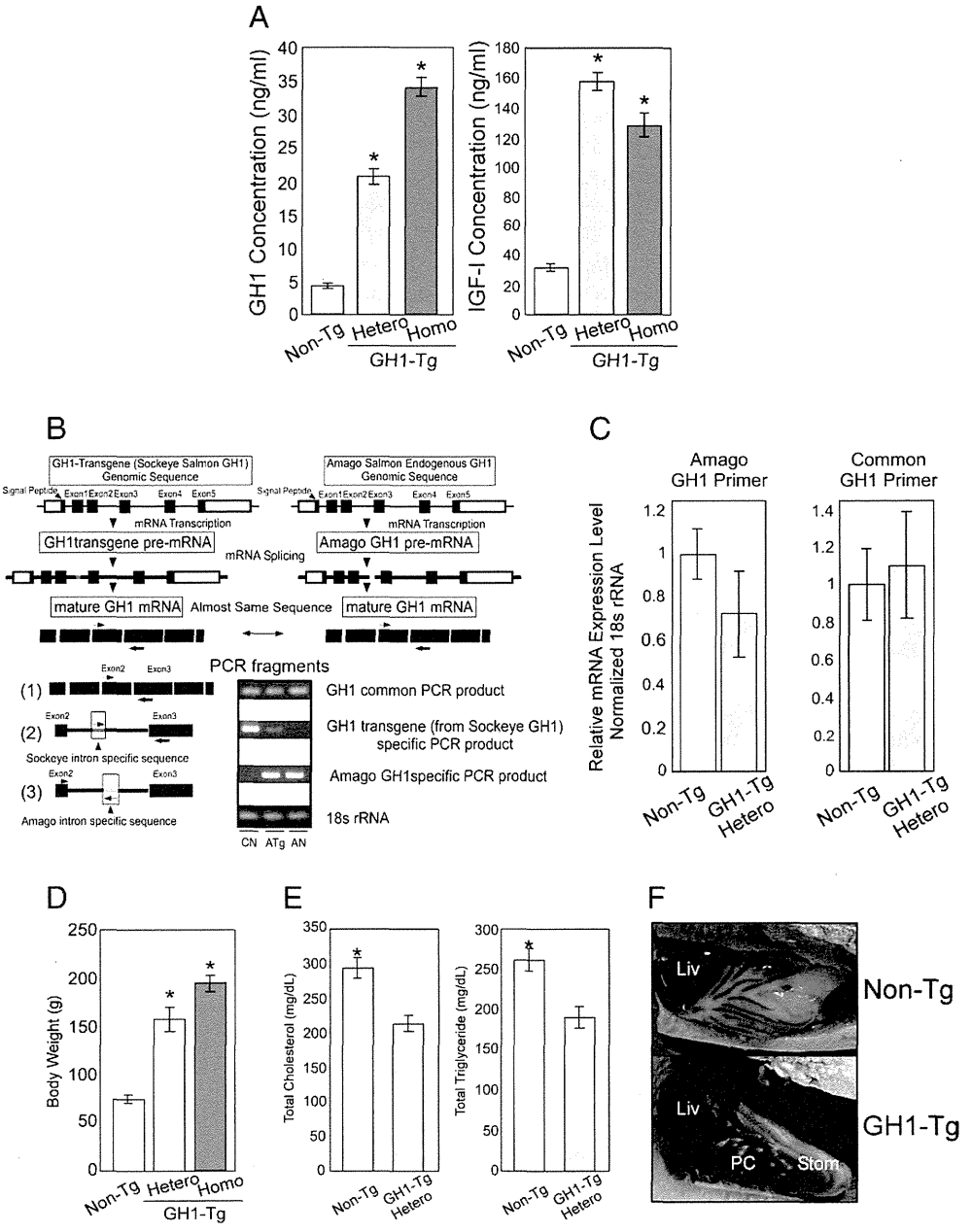

Fig. 3 – Characteristics of transgenic amago salmon overexpressing type 1 growth hormone (GH1). (A) The concentration of GH1 and IGF-I in plasma. GH1 and IGF-I levels in plasma were determined by ^{125}I-based radioimmuno assay. (B) Exon–intron structure of GH1-transgene (sockeye salmon) and amago salmon GH1 gene. To distinguish between amago salmon endogenous GH1 gene and sockeye salmon transgenic GH1 gene, primer sets used in reverse transcription (RT) PCR were designed against the region between exon 2 and exon 3, as follows: (1) GH1 common primers, which amplify both genes; (2) GH1 transgene-specific primers, which amplify only the sockeye salmon transgenic GH1 gene; and (3) amago-specific primers, which amplify only the endogenous amago salmon GH1 gene, respectively. CN, ATg, and AN indicated non-Tg coho salmon (*Oncorhynchus kisutch*), GH1-Tg amago salmon integrated sockeye salmon GH1 gene, and non-Tg amago salmon, respectively. Coho salmon DNA was also used for positive control to GH1 transgene-specific (the sockeye salmon transgenic GH1) primers and negative control to amago-specific primers. (C) GH1 mRNA levels in the pituitary, determined by qRT-PCR using primer sets (1) and (3) described in Fig. 3B. (D) Comparison of body weights among GH1-Tg (homo- and heterozygous) amago and non-Tg amago. (E) Total cholesterol and triglyceride concentrations in plasma derived from GH1-Tg heterozygotes and non-Tg amago. (F) Representative visceral fat of non-Tg (top) and GH1-Tg heterozygous (bottom) amago. "Liv", "PC", and "Stom" indicate liver, pyloric caeca, and stomach, respectively. Asterisks denoted significant differences between non-Tg and GH1-Tg amago at $p<0.05$ by one-way ANOVA (A, D) or Student's t-test (C, E).

ATP synthase subunit β (ATP5B) is a catalytic core subunit of mitochondrial membrane ATP synthase, and plays a crucial role of mitochondrial oxidative phosphorylation (OXPHOS). In comparison with proliferating cells, quiescent cells exhibit a decrease in expression of glycolytic enzymes and an increase in expression of OXPHOS related enzymes [36–38]. In this study, we observed down-regulation of ALDOC, TPI1, and GAPDH, and up-regulation of ATP5B in the excess GH1-treated pituitary (Table 2). Reduction of ribosomal protein also causes attenuation of cell proliferation [39,40]. In the excess GH1-treated pituitary, 60S ribosomal protein P2 (RPLP2) and L24 (RPL24) were decreased (Table 2). Furthermore, an increase in ubiquitin-specific peptidase 7 (USP7), which is a deubiquitinating enzyme and stabilizes various proteins like p53, MDM2 p53-binding protein, and RE1-silencing transcription factor, is predicted to induce a reduction in cell proliferation and differentiation [41–43]. Inhibition of apoptosis inducing factor 1 (AIFM1), a flavoprotein with an oxidoreductase enzymatic activity, would induce cell cycle arrest and the suppression of cell proliferation [44]. A decrease in cold-inducible RNA-binding protein (CIRBP), an RNA-binding protein involved in a variety of stress response and disease processes in various cell types, would induce a reduction in cell proliferation, viability, and stress response ability [45,46]. The expression level of prothymosin α (PTMA), a nuclear acidic protein, is correlated to proliferation activity in a pituitary cell line (GH1 cell) [47]. In the excess GH1-treated pituitary, up-regulation of USP7 and down-regulation of AIFM1, CIRBP, and PTMA were detected (Table 2). Thus, our results suggest that GH1 treatment might cause cell cycle arrest and the suppression of cell proliferation in the salmon pituitary.

3.1.3. *Lipid metabolism*

In the excess GH1-treated pituitary, the expression levels of malic enzyme 3 (ME3) and fatty acid synthase (FASN), which are lipid metabolism-related enzymes, were altered. ME3 catalyzes the conversion of malate to pyruvate, producing NADPH [48]. FASN plays a role in *de novo* biogenesis of long-chain fatty acids via utilization of NADPH [49]. Thus, up-regulation of ME3 and down-regulation of FASN in the excess GH1-treated pituitary suggest that excess GH1 treatment induces cells to suppress lipid synthesis (Table 2).

3.2. *Protein profile in the GH1 transgenic salmon*

3.2.1. *Characteristics of GH1 transgenic salmon*

To confirm that protein dynamics in the excess GH1-treated pituitary are the same as those *in vivo*, we generated a GH1-Tg amago salmon. The GH1 transgene, consisting of a sockeye salmon GH1 gene under the control of the metallothionein B (MT-B) promoter, was integrated into the amago salmon genome, resulting in over-expression of GH1 throughout the whole body. In the plasma of GH1-Tg amago salmon (both homo- and heterozygous), the concentrations of GH1 and GH1-induced IGF-I were markedly elevated (Fig. 3A). To investigate the expression level of GH1 in the pituitary of GH1-Tg amago salmon, we performed qRT-PCR analysis using three primer sets: (1) GH1 common primer, (2) GH1 transgene (from sockeye salmon) specific primer, and (3) endogenous GH1 (from amago salmon) specific primer (Fig. 3B), which can detect a total GH1, GH1 from the transgene, and endogenous GH1, respectively (Fig. 3B). qRT-PCR analysis using these primer sets indicated that, in the pituitary, GH1 transgenesis has an insignificant effect on total of GH1, because endogenous GH1 expression is down-regulated by *in vivo* GH1 regulation system that is activated by the increase in the level of transgenic GH1 (Fig. 3C). However, GH1 transgenesis had a variety of effects on the phenotypes of GH1-Tg amago salmon. Compared to non-Tg amago salmon, the average body weights of heterozygous and homozygous GH1-Tg individual were ~2- and 3-

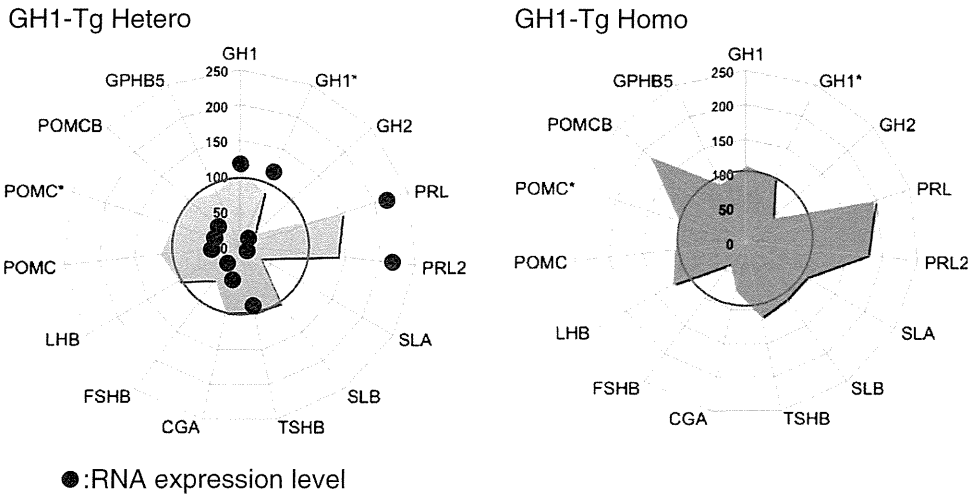

Fig. 4 – Comparison of expression levels of pituitary hormones in the GH1-Tg (homo- and heterozygous) and non-Tg pituitary by proteome and transcriptome analysis. Blue and red charts show that expression levels of pituitary hormones detected by proteome analysis in the pituitary of GH1-Tg (homo- and heterozygous). Asterisks indicate isoforms of identical pituitary hormones. Red circles indicate expression levels of pituitary hormones in non-Tg pituitary. Blue dots indicate expression levels of pituitary hormones obtained from subtractive microarray analysis. Each level represents the average among spots corresponding to each hormone gene. GH1/GH2 and PRL/PRL2 have highly similar sequences within each pair.

fold larger, respectively (Fig. 3D). In addition, GH1-Tg amago salmon exhibited enhancement of feeding behavior, shrinkage of the pituitary, and reduction of fertility, as do other GH1-Tg fish [5,17,50]. Furthermore, levels of total triglyceride and total cholesterol in the plasma of GH-Tg amago salmon were significantly decreased (Fig. 3E). Moreover, GH1-Tg amago salmon exhibited a reduction in visceral fat (Fig. 3F). These phenotypes were consistent with changes in protein expression levels observed in the excess GH1-treated pituitary.

3.2.2. *Identification of proteins and genes expressed in the GH1-Tg pituitary*

Proteins expressed specifically in the GH1-Tg pituitary were investigated by iTRAQ-MS/MS, resulting in the identification of 86 unique proteins that exhibit differential expression (≥1.25-fold change) in the GH1-Tg homozygous and/or heterozygous pituitary. Among them, 50 proteins did not change in the pituitary in response to excess GH1 treatment; 36 proteins were differentially regulated in excess GH1-treated pituitary. In the 36 proteins, the expression of the 28 proteins in the GH1-Tg homozygous and/or heterozygous pituitary showed similar pattern of the expression compared with excess GH1-treated pituitary, however, the expression of the remaining 8 proteins showed opposite expression pattern compared with that of excess GH1 treatment (Supplementary Table 1). The change in hormone balance in the GH1-Tg pituitary was almost identical to what was observed in the excess GH1-treated pituitary, except that SLA level did not change in the pituitary of the GH1-Tg homozygote (Figs. 2 and 4).

Additionally, we prepared customized amago salmon-specific subtractive microarrays using 1920 sequences (1915 amago cDNAs and 5 control DNAs). From the microarray analysis of mRNA levels in the pituitary, 45 genes (148 spots) listed in Supplementary Table 2 exhibited significant changes in the GH1-Tg amago heterozygote (fold change >1.5, $p<0.05$). The GH-Tg pituitary exhibited up-regulation of PRL/PRL2 and down-regulation of GH2, SLA, CGA and FSHB, just as in the excess GH1-treated pituitary; the mRNA levels of POMC and POMCB were markedly down-regulated (Fig. 4). These results were consistent with the down-regulation of GH gene expression in the pituitary from GH1-Tg salmon [50]. Bioinformatic analysis suggested that most of these differentially regulated molecules are involved in endocrine systems, metabolism, cell growth and proliferation (Supplementary Fig. 2).

4. Conclusion

In this study, excess GH1 treatment induced differential expression of pituitary proteins involved in endocrine systems, metabolism, cell proliferation and growth. In addition, the same protein dynamics were observed in the pituitary of GH1-Tg amago salmon. Furthermore, the characteristics predicted from these protein dynamics corresponded to the phenotypes of GH1-Tg salmon; these include enhancement of somatic growth and feeding behavior, shrinkage of the pituitary, reduction of fertility, and imbalances of lipid metabolism. Based on the results described above, we hypothesize that the regulation of hormone production and lipid metabolism are important to the enhancement of salmon somatic growth in response to GH1 treatment for the purpose of productivity improvement.

Supplementary materials related to this article can be found online at doi:10.1016/j.jprot.2011.12.009.

Acknowledgments

We are grateful to Dr. Hironori Ando for the technical advice about pituitary organ culture and to Dr. Koichiro Kano and Dr. Yoshinao Oki for IPA support. This work was supported in part by the Special Coordination Funds for Promoting Science and Technology "Creation of Innovation Centers for Advanced Interdisciplinary Research Areas" (to H.H.) and in part by the special subsidies for private school of Japan 14360104 (to T.M.) and Japanese grants 17380120 (to T.M. and H.H.) from the Ministry of Education, Culture, Sports, Science, and Technology, Japan.

REFERENCES

[1] Weltzien FA, Norberg B, Helvik JV, Andersen Ø, Swanson P, Andersson E. Identification and localization of eight distinct hormone-producing cell types in the pituitary of male Atlantic halibut (*Hippoglossus hippoglossus* L.). Comp Biochem Physiol A Mol Integr Physiol 2003;134:315–27.
[2] Ooi GT, Tawadros N, Escalona RM. Pituitary cell lines and their endocrine applications. Mol Cell Endocrinol 2004;228:1–21.
[3] Breves JP, Seale AP, Helms RE, Tipsmark CK, Hirano T, Grau EG. Dynamic gene expression of GH/PRL-family hormone receptors in gill and kidney during freshwater-acclimation of Mozambique tilapia. Comp Biochem Physiol A Mol Integr Physiol 2011;158:194–200.
[4] Ben-Jonathan N, Hugo ER, Brandebourg TD, LaPensee CR. Focus on prolactin as a metabolic hormone. Trends Endocrinol Metab 2006;17:110–6.
[5] Sundström LF, Devlin RH, Johnsson JI, Biagi CA. Vertical position reflects increased feeding motivation in growth hormone transgenic coho salmon (*Oncorhynchus kisutch*). Ethology 2003;109:701–12.
[6] Sambroni E, Abdennebi-Najar L, Remy JJ, Le Gac F. Delayed sexual maturation through gonadotropin receptor vaccination in the rainbow trout *Oncorhynchus mykiss*. Gen Comp Endocrinol 2009;164:107–16.
[7] Wong AO, Zhou H, Jiang Y, Ko WK. Feedback regulation of growth hormone synthesis and secretion in fish and the emerging concept of intrapituitary feedback loop. Comp Biochem Physiol A Mol Integr Physiol 2006;144:284–305.
[8] Agellon LB, Davies SL, Lin CM, Chen TT, Powers DA. Rainbow trout has two genes for growth hormone. Mol Reprod Dev 1988;1:11–7.
[9] Mori T, Deguchi F, Ueno K. Differential expression of Gh1 and Gh 2 genes by competitive RT-PCR in rainbow trout pituitary. Gen Comp Endocrinol 2001;123:137–43.
[10] Melmed S. Acromegaly pathogenesis and treatment. J Clin Invest 2009;119:3189–202.
[11] Perrini S, Laviola L, Carreira MC, Cignarelli A, Natalicchio A, Giorgino F. The GH/IGF1 axis and signaling pathways in the muscle and bone: mechanisms underlying age-related skeletal muscle wasting and osteoporosis. J Endocrinol 2010;205:201–10.
[12] Rius-Francino M, Acerete L, Jiménez-Amilburu V, Capilla E, Navarro I, Gutiérrez J. Differential effects on proliferation of GH and IGFs in sea bream(*Sparus aurata*) cultured myocytes. Gen Comp Endocrinol 2011;172:44–9.

[13] Madsen K, Friberg U, Roos P, Edén S, Isaksson O. Growth hormone stimulates the proliferation of cultured chondrocytes from rabbit ear and rat rib growth cartilage. Nature 1983;304:545–7.
[14] Johnsson Jorgen I, Bjornsson Bjorn Th. Growth hormone increases growth rate, appetite and dominance in juvenile rainbow trout, *Oncorhynchus mykiss*. Anim Behav 1994;48:177–86.
[15] Devlin RH, Sakhrani D, Tymchuk WE, Rise ML, Goh B. Domestication and growth hormone transgenesis cause similar changes in gene expression in coho salmon (*Oncorhynchus kisutch*). Proc Natl Acad Sci USA 2009;106: 3047–52.
[16] Devlin RH, Biagi CA, Yesaki TY. Growth, viability and genetic characteristics of GH transgenic coho salmon strains. Aquaculture 2004;236:607–32.
[17] Rahman MA, Mak R, Ayad H, Smith A, Maclean N. Expression of a novel piscine growth hormone gene results in growth enhancement in transgenic tilapia (*Oreochromis niloticus*). Transgenic Res 1998;7:357–69.
[18] Sheridan MA. Effects of thyroxin, cortisol, growth hormone, and prolactin on lipid metabolism of coho salmon, *Oncorhynchus kisutch*, during smoltification. Gen Comp Endocrinol 1986;64:220–38.
[19] Krasnov A, Agren JJ, Pitäknen TI, Mölsä H. Transfer of growth hormone (GH)transgenes into Arctic charr. (*Salvelinus alpinus* L.) II. Nutrient partitioning in rapidly growing fish. Genet Anal 1999;15:99–105.
[20] Falcón J, Besseau L, Fazzari D, Attia J, Gaildrat P, Beauchaud M, et al. Melatonin modulates secretion of growth hormone and prolactin by trout pituitary glands and cells in culture. Endocrinology 2003;144:4648–58.
[21] Shilov IV, Seymour SL, Patel AA, Loboda A, Tang WH, Keating SP, et al. The Paragon Algorithm, a next generation search engine that uses sequence temperature values and feature probabilities to identify peptides from tandem mass spectra. Mol Cell Proteomics 2007;6:1638–55.
[22] Tang WH, Shilov IV, Seymour SL. Nonlinear fitting method for determining local false discovery rates from decoy database searches. J Proteome Res 2008;7:3661–7.
[23] Mori T, Hiraka I, Kurata Y, Kawachi H, Mano N, Devlin RH, et al. Changes in hepatic gene expression related to innate immunity, growth and iron metabolism in GH-transgenic amago salmon (*Oncorhynchus masou*) by cDNA subtraction and microarray analysis, and serum lysozyme activity. Gen Comp Endocrinol 2007;151:42–54.
[24] Shimizu M, Swanson P, Fukada H, Hara A, Dickhoff WW. Comparison of extraction methods and assay validation for salmon insulin-like growth factor-I using commercially available components. Gen Comp Endocrinol 2000;119:26–36.
[25] Swanson P. Radioimmunoassay of fish growth hormone, prolactin, and somatolactin. In: Hochachka PW, Mommsen TP, editors. Analytical Techniques. Biochemistry and Molecular Biology of Fishes. Amsterdam: Elsevier Inc; 1994. p. 545–56.
[26] Moriyama S, Swanson P, Nishii M, Takahashi A, Kawauchi H, Dickhoff WW, et al. Development of a homologous radioimmunoassay for coho salmon insulin-like growth factor-I. Gen Comp Endocrinol 1994;96:149–61.
[27] Mori T, Kawachi H, Imai C, Sugiyama M, Kurata Y, Kishida O, et al. Identification of a novel uromodulin-like gene related to predator-induced bulgy morph in anuran tadpoles by functional microarray analysis. PLoS One 2009;4:e5936.
[28] Jiang Q, Ko WK, Lerner EA, Chan KM, Wong AO. Grass carp somatolactin: I. Evidence for PACAP induction of somatolactin-alpha and -beta gene expression via activation of pituitary PAC-I receptors. Am J Physiol Endocrinol Metab 2008;295:E463–76.
[29] Manzon LA. The role of prolactin in fish osmoregulation: a review. Gen Comp Endocrinol 2002;125:291–310.
[30] Chitalia VC, Foy RL, Bachschmid MM, Zeng L, Panchenko MV, Zhou MI, et al. Jade-1 inhibits Wnt signalling by ubiquitylating beta-catenin and mediates Wnt pathway inhibition by pVHL. Nat Cell Biol 2008;10:1208–16.
[31] Waite E, Lafont C, Carmignac D, Chauvet N, Coutry N, Christian H, et al. Different degrees of somatotroph ablation compromise pituitary growth hormone cell network structure and other pituitary endocrine cell types. Endocrinology 2010;151:234–43.
[32] Haisenleder DJ, Burger LL, Aylor KW, Dalkin AC, Marshall JC. Gonadotropin-releasing hormone stimulation of gonadotropin subunit transcription: evidence for the involvement of calcium/calmodulin-dependent kinase II (Ca/CAMKII) activation in rat pituitaries. Endocrinology 2003;144:2768–74.
[33] Wong AO, Li W, Leung CY, Huo L, Zhou H. Pituitary adenylate cyclase-activating polypeptide (PACAP) as a growth hormone (GH)-releasing factor in grass carp. I. Functional coupling of cyclic adenosine 3′,5′-monophosphate and Ca2+/calmodulin-dependent signaling pathways in PACAP-induced GH secretion and GH gene expression in grass carp pituitary cells. Endocrinology 2005;146:5407–24.
[34] Zhu X, Zhou A, Dey A, Norrbom C, Carroll R, Zhang C, et al. Disruption of PC1/3 expression in mice causes dwarfism and multiple neuroendocrine peptide processing defects. Proc Natl Acad Sci USA 2002;99:10293–8.
[35] Jackson RS, Creemers JW, Ohagi S, Raffin-Sanson ML, Sanders L, Montague CT, et al. Obesity and impaired prohormone processing associated with mutations in the human prohormone convertase 1 gene. Nat Genet 1997;16:303–6.
[36] López-Ríos F, Sánchez-Aragó M, García-García E, Ortega AD, Berrendero JR, Pozo-Rodríguez F, et al. Loss of the mitochondrial bioenergetic capacity underlies the glucose avidity of carcinomas. Cancer Res 2007;67:9013–7.
[37] Vander Heiden MG, Cantley LC, Thompson CB. Understanding the Warburg effect: the metabolic requirements of cell proliferation. Science 2009;324:1029–33.
[38] Cai Z, Zhao JS, Li JJ, Peng DN, Wang XY, Chen TL, et al. A combined proteomics and metabolomics profiling of gastric cardia cancer reveals characteristic dysregulations in glucose metabolism. Mol Cell Proteomics 2010;9: 2617–28.
[39] Chen A, Kaganovsky E, Rahimipour S, Ben-Aroya N, Okon E, Koch Y. Two forms of gonadotropin-releasing hormone (GnRH) are expressed in human breast tissue and overexpressed in breast cancer: a putative mechanism for the antiproliferative effect of GnRH by down-regulation of acidic ribosomal phosphoproteins P1 and P2. Cancer Res 2002;62:1036–44.
[40] Barna M, Pusic A, Zollo O, Costa M, Kondrashov N, Rego E, et al. Suppression of Myc oncogenic activity by ribosomal protein haploinsufficiency. Nature 2008;456: 971–5.
[41] Li M, Chen D, Shiloh A, Luo J, Nikolaev AY, Qin J, et al. Deubiquitination of p53 by HAUSP is an important pathway for p53 stabilization. Nature 2002;416:648–53.
[42] Li M, Brooks CL, Kon N, Gu W. A dynamic role of HAUSP in the p53-Mdm2 pathway. Mol Cell 2004;13:879–86.
[43] Huang Z, Wu Q, Guryanova OA, Cheng L, Shou W, Rich JN, et al. Deubiquitylase HAUSP stabilizes REST and promotes maintenance of neural progenitor cells. Nat Cell Biol 2011;13: 142–52.
[44] Schulthess FT, Katz S, Ardestani A, Kawahira H, Georgia S, Bosco D, et al. Deletion of the mitochondrial flavoprotein apoptosis inducing factor(AIF) induces

beta-cell apoptosis and impairs beta-cell mass. PLoS One 2009;4:e4394.
[45] Artero-Castro A, Callejas FB, Castellvi J, Kondoh H, Carnero A, Fernández-Marcos PJ, et al. Cold-inducible RNA-binding protein bypasses replicative senescence in primary cells through extracellular signal-regulated kinase 1 and 2 activation. Mol Cell Biol 2009;29:1855–68.
[46] Zeng Y, Kulkarni P, Inoue T, Getzenberg RH. Down-regulating cold shock protein genes impairs cancer cell survival and enhances chemosensitivity. J Cell Biochem 2009;107:179–88.
[47] Alvarez CV, Zalvide JB, Cancio E, Dieguez C, Regueiro BJ, Vega FV, et al. Regulation of prothymosin alpha mRNA levels in rat pituitary tumor cells. Neuroendocrinology 1993;57: 1048–56.
[48] DeBerardinis RJ, Lum JJ, Hatzivassiliou G, Thompson CB. The biology of cancer: metabolic reprogramming fuels cell growth and proliferation. Cell Metab 2008;7:11–20.
[49] Menendez JA, Lupu R. Fatty acid synthase and the lipogenic phenotype in cancer pathogenesis. Nat Rev Cancer 2007;7: 763–77.
[50] Mori T, Devlin RH. Transgene and host growth hormone gene expression in pituitary and nonpituitary tissues of normal and growth hormone transgenic salmon. Mol Cell Endocrinol 1999;149:129–39.

THE JOURNAL OF BIOLOGICAL CHEMISTRY VOL. 287, NO. 22, pp. 18710–18716, May 25, 2012

Structural Basis for Inhibition of Xyloglucan-specific Endo-β-1,4-glucanase (XEG) by XEG-Protein Inhibitor*

Received for publication, February 7, 2012 and in revised form, April 9, 2012 Published, JBC Papers in Press, April 10, 2012, DOI 10.1074/jbc.M112.350520

Takuya Yoshizawa (吉澤 拓也)[‡], **Toshiyuki Shimizu** (清水 敏之)[§], **Hisashi Hirano** (平野 久)[‡], **Mamoru Sato** (佐藤 衛)[‡], **and Hiroshi Hashimoto** (橋本 博)[‡1]

From the [‡]Graduate School of Nanobioscience, Yokohama City University, 1-7-29 Suehiro-cho, Tsurumi-ku, Yokohama, Kanagawa 230-0045, Japan and the [§]Graduate School of Pharmaceutical Science, The University of Tokyo, 7-3-1 Hongo, Bunkyo-ku, Tokyo 113-0033, Japan

Background: Plants produce glycoside hydrolase inhibitor protein to protect cell walls.
Results: The inhibition mechanism for a xyloglucanase-inhibitor of a fungal xyloglucanase is revealed by crystal structures.
Conclusion: Xyloglucanase inhibitor protein distinguishes specific structural features of a glycosyl hydrolase to protect the plant cell wall from degradation.
Significance: Understanding the mechanism of xyloglucanase inhibition is key to comprehending how plants defend themselves against microbes that express glycosyl hydrolases.

Microorganisms such as plant pathogens secrete glycoside hydrolases (GHs) to digest the polysaccharide chains of plant cell walls. The degradation of cell walls by these enzymes is a crucial step for nutrition and invasion. To protect the cell wall from these enzymes, plants secrete glycoside hydrolase inhibitor proteins (GHIPs). Xyloglucan-specific endo-β-1,4-glucanase (XEG), a member of GH family 12 (GH12), could be a great threat to many plants because xyloglucan is a major component of the cell wall in most plants. Understanding the inhibition mechanism of XEG by GHIP is therefore of great importance in the field of plant defense, but to date the mechanism and specificity of GHIPs remain unclear. We have determined the crystal structure of XEG in complex with extracellular dermal glycoprotein (EDGP), a carrot GHIP that inhibits XEG. The structure reveals that the conserved arginines of EDGP intrude into the active site of XEG and interact with the catalytic glutamates of the enzyme. We have also determined the crystal structure of the XEG-xyloglucan complex. These structures show that EDGP closely mimics the XEG-xyloglucan interaction. Although EDGP shares structural similarity to a wheat GHIP (*Triticum aestivum* xylanase inhibitor-IA (TAXI-IA)) that inhibits GH11 family xylanases, the arrangement of GH and GHIP in the XEG-EDGP complex is distinct from that in the xylanase-TAXI-IA complex. Our findings imply that plants have evolved structures of GHIPs to inhibit different GH family members that attack their cell walls.

Plant cell walls are composed of various polysaccharides such as cellulose, hemicellulose, and pectin. In most plant cell wall models, cellulose microfibrils are linked via hemicellulose. This cellulose-hemicellulose network provides tensile strength and acts as a physical barrier against microorganisms such as invading pathogens. To penetrate and utilize plant cell walls nutritionally, microorganisms secrete hydrolases for cell wall degradation. These enzymes, which include endoglucanases, xylanases, and polygalacturonases, are classified into glycoside hydrolase (GH)[2] families in the CAZY data base (1). In response to pathogenic attack, plants produce glycoside hydrolase inhibitor proteins (GHIPs) against the cell wall-degrading enzymes (2, 3).

Extracellular dermal glycoprotein (EDGP) from carrot is one such GHIP. EDGP shows inhibitory activity toward the xyloglucan-specific endo-β-1,4-glucanase (XEG) from the fungus *Aspergillus aculeatus* (4). EDGP is alternatively called XEG inhibitor protein (XEGIP). XEG belongs to GH family 12 (GH12) and specifically cleaves xyloglucan, which consists of a β-linked glucose backbone substituted with xylose side chains (5). Xyloglucan is a major hemicellulose in most plants (6), and thus xyloglucanases such as XEG are a great threat to plants because the degradation of hemicellulose causes great damage. The inhibition of XEG by EDGP is an important component of the plant defense system. Proteins homologous to EDGP have been identified in various plants, and several of these proteins have been characterized. Tomato XEGIP inhibits XEG by forming an associated 1:1 complex (7). Tobacco Necturin IV (NEC IV) also inhibits XEG (8). In contrast, the homologous protein from wheat, TAXI-IA (*Triticum aestivum* xylanase inhibitor-IA), inhibits a GH family 11 (GH11) xylanase from fungus, ANXI (*Aspergillus niger* xylanase I) (9–11). Interestingly, the homologous protein from soybean, basic 7S globulin (Bg7S), lacks inhibitory activity for either GH11 or GH12 enzymes (12).

* This work was supported by a Grant-in-Aid for Scientific Research (KAKENHI), the National Project on Protein Structural and Functional Analyses Protein 3000 Project, and the Targeted Proteins Research Program from Ministry of Education, Culture, Sports, Science, and Technology in Japan (MEXT) (to T. S., M. S., and H. H.).

The atomic coordinates and structure factors (codes 3VL8, 3VL9, 3VLA, and 3VLB) have been deposited in the Protein Data Bank, Research Collaboratory for Structural Bioinformatics, Rutgers University, New Brunswick, NJ (http://www.rcsb.org/).

[1] To whom correspondence should be addressed. Tel.: 81-45-508-7227; Fax: 81-45-508-7365; E-mail: hash@tsurumi.yokohama-cu.ac.jp.

[2] The abbreviations used are: GH, glycoside hydrolase; ANXI, *Aspergillus niger* xylanase I; Bg7S, basic 7S globulin; EDGP, extracellular dermal glycoprotein; GHIP, GH inhibitor protein; IL, inhibition loop; PDB, Protein Data Bank; TAXI-IA, *Triticum aestivum* xylanase inhibitor-IA; XEG, xyloglucan-specific endo-β-1,4-glucanase; XEGIP, XEG inhibitor protein; FI-CMCase, FI-carboxymethyl cellulose.

The crystal structures of the ANXI-TAXI-IA complex and Bg7S have been determined (10, 12). However, not only the inhibition mechanism of XEG but also the mechanism underlying family-specific inhibition by GHIP have remained unclear.

In this work, we have determined the crystal structures of XEG, the XEG-xyloglucan complex, EDGP, and the XEG-EDGP complex. The structure of the XEG-xyloglucan complex provides a structural basis of specific recognition of xyloglucan by XEG. The structure of the XEG-EDGP complex reveals how GHIP recognizes the active site of GH12 and inhibits its activity. Surprisingly, the arrangement of GH and GHIP in the XEG-EDGP complex is distinct from that in the ANXI-TAXI-IA complex. Our findings clarify the mechanism of family-specific inhibition of GH12 and GH11 by EDGP homologous GHIPs.

EXPERIMENTAL PROCEDURES

Preparation of EDGP and XEG—The preparation of EDGP and XEG has been described previously (12, 13). In brief, EDGP was purified from carrot callus culture medium. The carrot callus was grown for 2–3 weeks at 298 K in Murashige-Skoog medium containing 1 mg/liter 2,4-dichlorophenoxyacetic acid. The protein was purified using HiTrap SP (GE Healthcare). The cDNA encoding XEG was obtained by PCR-based gene synthesis (14) and inserted into pGEX6P-I vector (GE Healthcare) at the BamHI-XhoI site. N-terminal GST-fused XEG was expressed in *Escherichia coli* BL21. The protein was purified using glutathione-Sepharose 4B resin (GE Healthcare), a HiTrap Q HP column (GE Healthcare), and a HiLoad Superdex 75 26/60 column (GE Healthcare).

Enzyme Activity Assay—The activity of XEG wild-type or mutants was measured using *p*-hydroxybenzoic acid hydrazide (PAHBAH) method (15). The reaction mixture contained 50 mM sodium acetate, pH 4.6, 100 mM NaCl, 5 mg/ml xyloglucan from tamarind seeds (DS Pharma), and 100 ng of XEG in the absence or presence of 5 μg of EDGP. The final reaction volume was 20 μl. The reaction mixtures were incubated at room temperature for 15 min, and then the amount of reducing sugar was measured.

Crystallographic Analyses—All crystals were obtained by the hanging-drop vapor diffusion method at 293 K. Hexagonal crystals of XEG were obtained under 0.1 M sodium acetate, pH 5.5, and 1.5 M ammonium sulfate. The co-crystal of XEG-xyloglucan was obtained under 0.1 M sodium acetate, pH 4.6, 25% PEG 3000, and 5 mg/ml digested xyloglucan. XEG used in crystallization with xyloglucan was wild type. The preparation of digested xyloglucan has been described previously (16). Hexagonal crystals of EDGP were obtained under 0.2 M ammonium acetate, 0.1 M sodium acetate, pH 4.6, and 30% PEGMME2000. Iodine-derived crystals of EDGP were prepared by the vaporizing iodine labeling method (17). A droplet of iodine solution (0.67 M KI and 0.47 M I_2) was placed next to the crystallization droplet containing EDGP crystals. After 20 min, the iodine solution was removed and the crystallization droplet was incubated for a further 20 h.

To crystallize the XEG-EDGP complex, XEG protein with an N-terminal truncation, XEG(8–224), was prepared. The XEG-EDGP complex was prepared by mixing EDGP and XEG(8–224) in an equal molar ratio. Monoclinic crystals of the XEG-EDGP complex were obtained under 0.24 M Morpheus alcohols (Molecular Dimensions), 0.1 M Morpheus Buffer system 3, pH 8.5 (Molecular Dimensions), 30% Morpheus EOD_P8K (Molecular Dimensions), and 9% dextran sulfate.

X-ray diffraction data for crystals of XEG, XEG-xyloglucan, EDGP native, EDGP derivative, and XEG-EDGP were collected in-house at UltraX18 (Rigaku), Photon Factory (PF) BL-17A, SPring-8 BL-41XU, PF NE-3A, and SPring-8 BL-32XU, respectively. All diffraction data were processed using the program HKL2000 (18). The XEG structure was solved by the molecular replacement method with the program MOLREP (19) using the endo-β-1,4-glucanase from *Hypocrea jecorina* as a search model (Protein Data Bank (PDB) ID code 1OA2). The EDGP structure was solved by the SIRAS method using the programs SOLVE and RESOLVE (20). The EDGP-XEG complex structure was solved by the molecular replacement method with the program MOLREP (19) using EDGP and XEG structures as search models. Model building was performed with the program COOT (21). Structure refinement was performed with the programs CNS (22) and REFMAC (23). The geometries of the final structures were validated with the program PROCHECK (24). Data collection and refinement statistics are given in Table 1. Final coordinates and structure factors have been deposited in the Protein Data Bank Japan (PDBj).

Pulldown Assay—GST-fused XEG and its mutants were overexpressed in *E. coli* BL21 and purified by glutathione-Sepharose 4B resin. Next, EDGP and GST-fused XEG were incubated with glutathione-Sepharose 4B beads equilibrated with a buffer containing 50 mM sodium acetate, pH 4.6, and 100 mM NaCl for 1 h at 25 °C. The beads were washed with the above buffer and eluted with a buffer containing 100 mM Tris-HCl, pH 9.0, 200 mM NaCl, and 50 mM reduced glutathione. The GST tags were cleaved by HRV3C protease. The proteins in solution were analyzed by SDS-PAGE with Coomassie Brilliant Blue staining. Band intensities were calculated by the program ImageJ (National Institutes of Health).

Figure Preparation—Protein structures were prepared with the program PyMOL (DeLano Scientific). All of the figures were modified with the programs PHOTOSHOP and ILLUSTRATOR (Adobe Systems).

RESULTS

Structure of XEG-Xyloglucan Complex—We determined the crystal structures of XEG and XEG in complex with xyloglucan at 1.9 and 1.2 Å resolution, respectively. The structure of XEG bound to xyloglucan could be superimposed on that of XEG, with a root mean square deviation value of 0.6 Å for comparable Cα atoms. XEG adopts a β-jelly roll fold, as observed in other enzymes of the family GH12 (25). A cleft runs across the surface of the protein, and the xyloglucan-binding subsites are located within this cleft. The hydrolysis reaction of the GH12 enzymes proceeds with a two-step retaining mechanism catalyzed by two glutamate residues: one acts as the nucleophile and the other as the acid/base (25). The putative nucleophile and acid/base in XEG are Glu^{119} and Glu^{205}, respectively. The electron density map clearly shows binding of xyloglucan within the cleft, where the β-1,4-glucose backbone is bound to the -1 to

TABLE 1
Data collection and refinement statistics

Parameters	XEG	XEG-xyloglucan	EDGP	EDGP deriv	XEG-EDGP
Data collection					
Wavelength (Å)	1.5418	1.0000	0.8000	1.900	1.0000
Space group	$P6_5$	$P2_12_12_1$	$P6_2$	$P6_2$	$C2$
a (Å)	93.0	62.6	130.1	130.1	249.0
b (Å)	93.0	79.3	130.1	130.1	51.7
c (Å)	62.0	80.4	44.5	44.5	143.2
α (°)	90	90	90	90	90
β (°)	90	90	90	90	122.2
γ (°)	120	90	120	120	90
Resolution (Å)	50.0–1.90	50.0–1.20	50–0.92	50.0–2.40	50.0–2.70
Observed reflections	134,050	743,148	1,283,262	343,185	121,934
Unique reflections	24,103	120,607	272,047	16,855	40,308
R-merge (%)	8.3 (31.6)	6.9 (31.7)	7.5 (32.6)	6.4 (21.8)	7.8 (38.4)
Completeness (%)	99.6 (98.8)	95.8 (75.2)	91.6 (74.3)	98.2 (95.2)	91.9 (83.2)
$<I>/\sigma<I>$	14.8 (7.0)	12.8 (3.3)	12.2 (2.0)	19.2 (11.3)	12.4 (3.3)
Refinement					
Resolution (Å)	1.90	1.20	0.95		2.70
Refined reflections	22,833	114,328	239,679		37,707
Free reflections	1,142	5,716	11,983		1,885
R (%)	18.0	12.3	12.6		25.2
R-free (%)	21.2	16.2	14.5		33.9
Root mean square deviation					
Bond length (Å)	0.005	0.015	0.016		0.015
Bond angles (°)	0.951	1.637	1.782		1.823
Ramachandran plot					
Most favored (%)	93.7	92.7	89.3		82.3
Additional allowed (%)	5.8	7.3	10.1		16.4
Generously allowed (%)	0.5	0.0	0.3		0.8
Disallowed (%)	0.0	0.0	0.3		0.5
Protein Data Bank ID code	3VL8	3VL9	3VLA		3VLB

−4 subsites, and α-1,6-xylose residues branching from the glucose moieties in subsites −2 and −3 are also observed in the electron density (Fig. 1*A*). Trp^{13} and Trp^{28} form hydrophobic interactions with the glucose moieties of the β-1,4-glucan chain in the −4 and −2 subsites, respectively (Fig. 1*B*). In addition to these hydrophobic interactions, the catalytic Glu^{119} and Glu^{205} residues form hydrogen bonds with oxygen atoms of the glucose moiety in the −1 subsite.

The XEG structure shows the structural basis for specific recognition of xyloglucan by the enzyme. Tyr^{24} stacks against the xylose side chain linked to the glucose moieties in the −3 subsite, and Glu^{201} interacts with the O5 oxygen atoms of xylose (Fig. 1*B*). To investigate which residues are responsible for XEG activity, we prepared XEG mutants and measured their xyloglucanase activity (Fig. 1*C*). An XEG mutant with a W13A, W28A, or W13A/W28A substitution(s) lacked almost all xyloglucanase activity, clearly indicating that these tryptophans, which are involved in the hydrophobic interaction with the glucose backbone, are essential for this activity. Remarkably, a Y24A substitution also markedly decreased the activity of XEG. Tyr^{24} of XEG is not conserved in the GH12 enzyme from *A. aculeatus*, FI-CMCase (26). FI-CMCase hydrolyzes carboxylmethylated β-1,4-glucan, a model substrate of cellulase, and cleaves xyloglucan with approximately half of the activity of XEG. These results suggest that a stacking interaction of a hydrophobic nature between Tyr^{24} and the xylose side chain is crucial for xyloglucan recognition. A previous study has revealed the crystal structure of a GH12 xyloglucanase from *Bacillus licheniformis* (BlXG12) in complex with xyloglucan (27). In this structure, tryptophan residues are involved in interactions with glucose backbone just as we observe with XEG. However, stacking interactions between an aromatic residue and a xylose residue were not observed. This is consistent with the fact that the BlXG12 also possesses glucanase activity to digest carboxymethyl cellulose (CMC) (27).

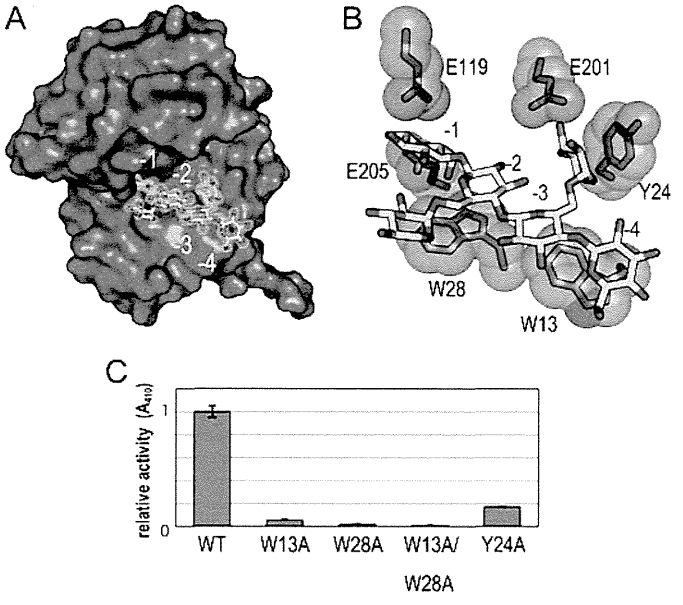

FIGURE 1. **Recognition of xyloglucan by XEG.** *A*, structure of XEG-xyloglcan complex. XEG and xyloglucan are represented by a *surface* and *stick models*, respectively. The observed electron density of xyloglucan is shown by *white mesh* ($2F_o - F_c$, 1σ). *B*, detailed interactions between XEG and xyloglucan are shown by *stick* and *sphere models*. Carbon of XEG, carbon of xyloglucan, oxygen, and nitrogen are colored *light blue*, *yellow*, *red*, and *blue*, respectively. *C*, activities of the XEG mutants were estimated relative to that of wild-type (*WT*).

Structure of EDGP—The crystal structure of carrot EDGP was determined at 0.95 Å resolution (Fig. 2*A*). In the structure, the N-terminal glutamine is converted to a pyroglutamic acid

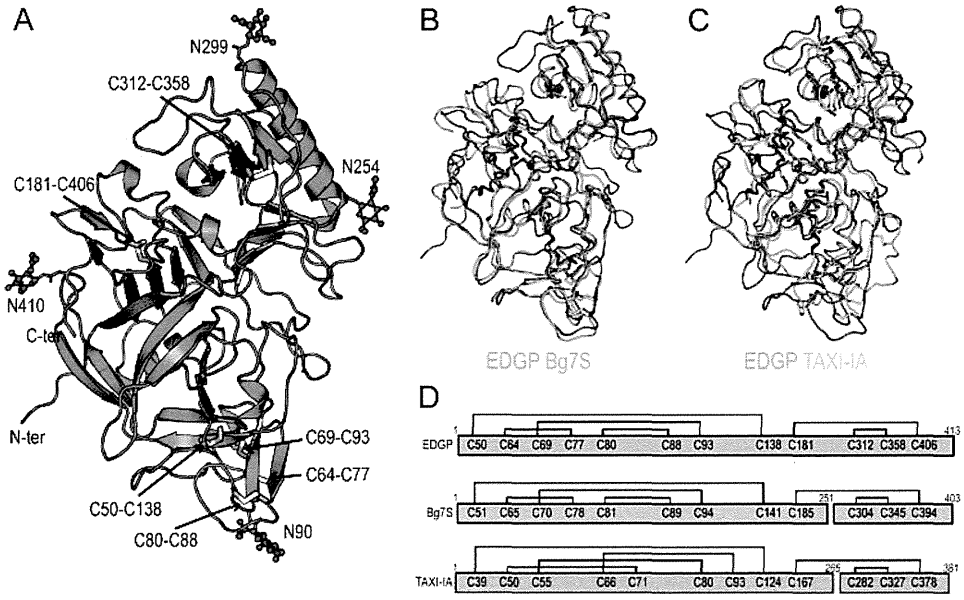

FIGURE 2. **Crystal structure of EDGP.** *A*, overall structure of EDGP is represented by a *ribbon model*. The disulfide bonds are shown by *stick models*, in which sulfur atoms are colored *yellow*. *N*-Linked glycans are represented by *ball* and *stick models* and colored *red*. *B*, superimposed structures of EDGP (*orange*) and Bg7S (*light green*) are represented as *wire models*. *C*, superimposed structures of EDGP (*orange*) and TAXI-IA (*cyan*) are represented as *wire models*. *D*, schematic drawing shows disulfide bonds in EDGP, Bg7S, and TAXI-IA.

(28). EDGP adopts a pepsin-like fold that is β-rich with several α-helices and is roughly divided by a center cleft comprising the active site (29). Despite the structural similarity to pepsin, one of the catalytic aspartates in pepsin is replaced by Ser^{271} in EDGP, and thus EDGP lacks protease activity. Consistent with this, other GHIPs also lack the catalytic aspartate. EDGP has six disulfide bonds, and these supposedly stabilize the tertiary structure of EDGP in the extracellular environment (Fig. 2, *A* and *D*). EDGP has four putative *N*-linked glycosylation sites: Asn^{90}, Asn^{254}, Asn^{299}, and Asn^{410} (28). In each putative *N*-linked glycosylation site, the electron density map indicated at least one sugar moiety linked to the asparagine (Fig. 2*A*).

The crystal structures of homologous proteins from wheat (TAXI-IA) and soybean (Bg7S) have been reported previously (10, 12). The overall structure of EDGP is similar to those of Bg7S and TAXI-IA. The root mean square deviation value for Cα atoms comparable with Bg7S (PDB ID code 3AUP) and TAXI-IA (PDB ID code 1T6E) is 1.6 and 2.4 Å, respectively (Fig. 2, *B* and *C*). EDGP, Bg7S, and TAXI-IA all have six disulfide bonds. Although the patterns of disulfide formation are conserved in EDGP and Bg7S, they differ from that in TAXI-IA (Fig. 2*D*). Bg7S and TAXI-IA undergo post-translational cleavage in their internal regions, whereas EDGP does not (Fig. 2*D*). The variation in post-translational modification of GHIPs is of interest, although the functional associations of these modifications in GHIPs remains unclear.

Structure of XEG-EDGP Complex, and Its Interaction—The crystal structure of XEG in complex with EDGP was determined at 2.7 Å resolution (Fig. 3*A*). The XEG-EDGP complex structure shows that EDGP completely covers the active cleft of XEG. The averaged root mean square deviations of comparable Cα atoms between each native structure (XEG and EDGP) and the XEG-EDGP complex are 0.8 and 0.7 Å, respectively, suggesting no substantial conformational changes occur in EDGP upon the binding of XEG. The calculated buried solvent-accessible surface area is 2046 $Å^2$ in the complex, comparable with that of the ANXI-TAXI-IA complex (1998 $Å^2$). We did not observe sugar chains at all of the *N*-linked glycosylation sites of EDGP because of ambiguity in the electron density map. In the XEG-EDGP structure, Arg^{322} and Arg^{403} of EDGP insert into the active cleft of XEG and form an electrostatic interaction with the catalytic residues, Glu^{119} and Glu^{205} (Fig. 3*B*). Hydrophobic interactions are made between the aliphatic moiety of Arg^{403} of EDGP and Trp^{28} of XEG, Leu^{202} and Pro^{203} of EDGP and Trp^{13} of XEG (Fig. 3*B*). To identify the amino acid residues of XEG responsible for the interaction with EDGP, we performed a pulldown assay using XEG mutants and EDGP (Fig. 3*C*). We did not observe a marked reduction in the interaction with EDGP with single or double mutations. However, mutations in residues involved in the interaction with EDGP weakened the binding ability, suggesting that both electrostatic and hydrophobic interactions are important in the interaction between XEG and EDGP (Fig. 3, *B* and *C*).

Structural overlay of the XEG-EDGP inhibition complex and the XEG-xyloglucan complex revealed the strategy employed by EDGP for inhibition (Fig. 4). Namely, the guanidium moieties of Arg^{322} and Arg^{403} of EDGP in the inhibition complex are located in the −1 subsite of XEG, and the aliphatic moiety of the side chain of Arg^{403} is located in the −2 subsite of XEG. Furthermore, Leu^{202} and Pro^{203} of EDGP, which are conserved in most plants, are located in the −4 subsite of XEG. These findings indicate that EDGP mimics the interaction between XEG and xyloglucan observed in the structure of the XEG-xyloglucan complex. Interestingly, EDGP does not interact with Tyr^{24} of XEG, which is involved in xylose recognition (Fig. 1*B*). The lack of any interaction with Tyr^{24} of XEG might be explained by our unpublished data that EDGP also inhibits the glucanase activity of FI-CMCase, which lacks this tyrosine res-

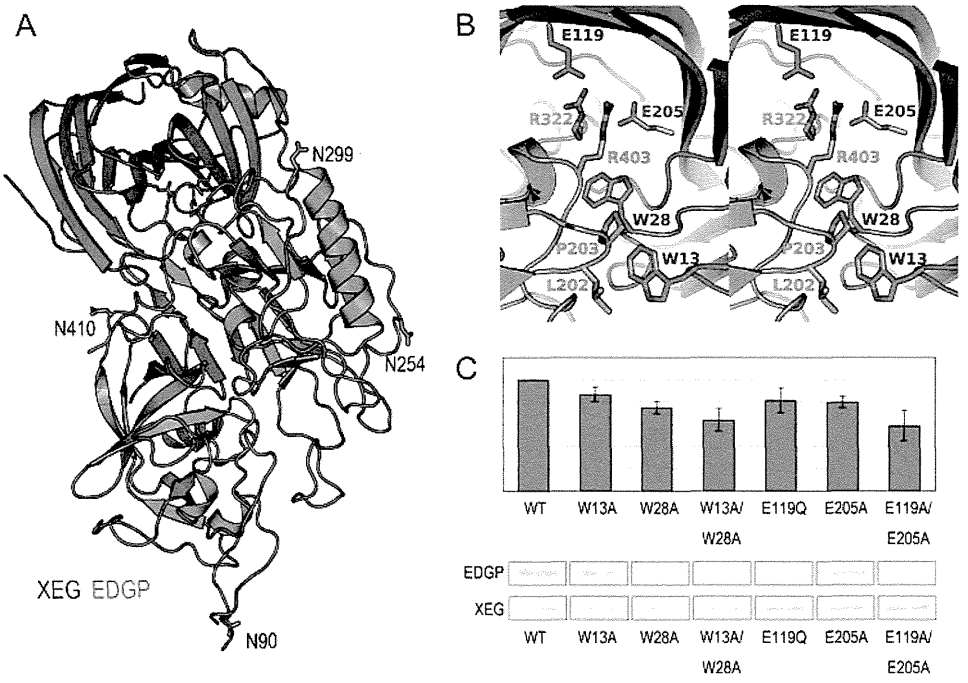

FIGURE 3. **Crystal structure of the XEG-EDGP inhibition complex and interactions between EDGP and XEG.** *A*, overall structure of inhibition complex of EDGP (*orange*) and XEG (*light blue*) shown by a *ribbon model*. *B*, stereo view of the detailed interactions between EDGP (*orange*) and XEG (*light blue*). *C*, binding activity of XEG mutants with EDGP (*upper panel*) estimated by band intensity of pulldown assay (*bottom panel*).

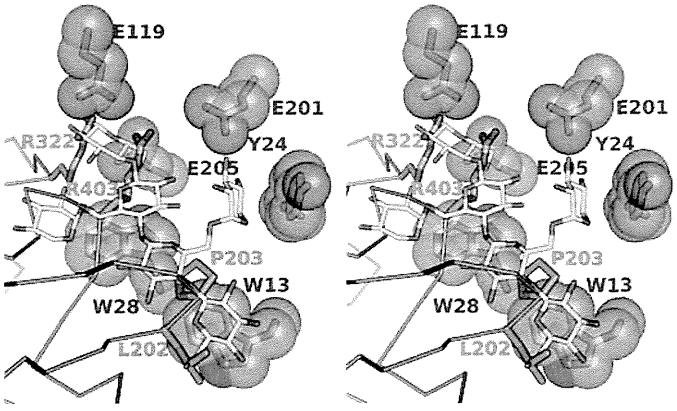

FIGURE 4. **Comparison between XEG-EDGP and XEG-xyloglucan interactions.** Stereo view shows XEG-EDGP interactions, with xyloglucan superimposed from the structure of XEG-xyloglucan. XEG (*light blue*), EDGP (*orange*), and xyloglucan (*yellow*) are shown by *stick and sphere*, *stick and wire*, and *stick models*, respectively.

idue. The EDGP complex with FI-CMCase has been crystallized (13) and solved.[3]

DISCUSSION

The crystal structure of the XEG-xyloglucan complex provides a structural basis for understanding the specific recognition of xyloglucan by XEG. The structure of the XEG-EDGP inhibition complex reveals details of the inhibition mechanism, in which two arginines located in inhibition loops 1 and 2 (IL-1 and IL-2) of EDGP intrude into the catalytic cleft of XEG and mimic the interactions formed between XEG and xyloglucan (Figs. 4 and 5*A*). The two arginines in IL-1 and IL-2 are conserved in most GHIPs, including homologous proteins from tomato, tobacco, potato, and *Arabidopsis* (Fig. 5*B*). Of these, tomato and tobacco GHIPs inhibit GH12 enzymes (7, 8). Furthermore, Leu^{202} and Pro^{203} (which contact the −4 subsite of the enzyme active site) are also conserved in GHIPs of most plants. Although the inhibitory activity of GHIP from potato or *Arabidopsis* has not been reported, our results suggest that these GHIPs might inhibit GH12 enzymes by means of their conserved arginines, leucine, and proline. In the GH11-TAXI-IA complex, Leu^{292} in IL-1 and His^{374} in IL-2 are involved in target-binding interactions. These residues are conserved in GHIPs of some monocots of the order Poales, including grasses, whose hemicellulose is xylan. Thus, rye GHIP might inhibit GH11 enzymes instead of GH12.

Structural overlays of EDGP and TAXI-IA in the GH-GHIP complexes reveal very similar positioning of IL-1 and IL-2 in these complexes (Fig. 5*A*), indicating that EDGP and TAXI-IA use similar regions to interact with their corresponding GHs. Although the overall structures of XEG and EDGP are comparable with those of ANXI and TAXI-IA (Fig. 2*C*), the arrangement of GH and GHIP in the XEG-EDGP complex is distinct from that in the ANXI-TAXI-IA complex (Fig. 5*C*). There is a small but significant difference between the XEG and ANXI structures. The structure of GH displaying the β-jelly roll fold including GH11 and GH12 has been likened to a right hand, with a thumb, palm, and fingers (30). The thumb or fingers forms a lid over the active site cleft in both ANXI and XEG (Fig. 5*C*). The putative model structure of an ANXI-EDGP or XEG-TAXI-IA complex built by superimposition of the GH structures clearly shows a steric clash between the lid of GH and GHIP (Fig. 5*D*). This indicates an intrinsic difference in the lid structures of ANXI and XEG which is conserved in each member of the GH11 and GH12 families. Therefore, our findings

[3] T. Yoshizawa, T. Shimizu, H. Hirano, M. Sato, and H. Hashimoto, unpublished data.

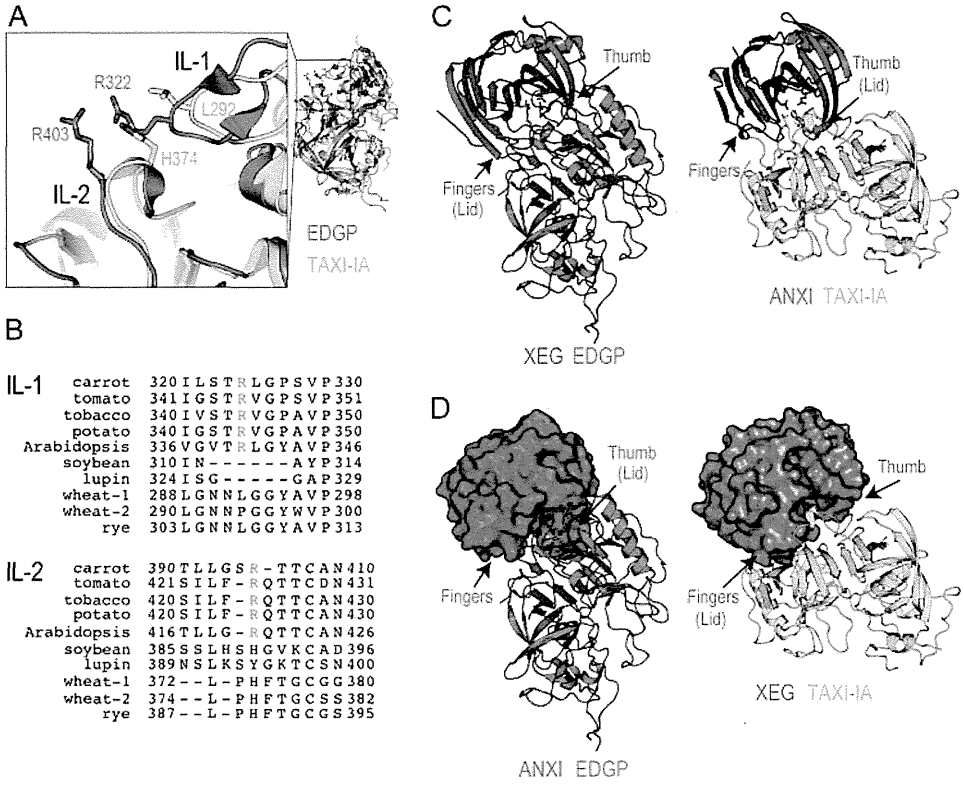

FIGURE 5. **Diverse mechanisms of target recognition of GH12 and GH11 by GHIP.** *A*, close-up view (*left*) around IL-1 and IL-2 of the superimposed structures (*right*) of EDGP (*orange*) and TAXI-IA (*cyan*). *B*, sequence alignment of IL-1 and IL-2 of EDGP with homologous proteins from various plants, tomato (UniProt ID; Q8GT67), tobacco (Q3KU27), potato (Q7XJE7), *Arabidopsis* (Q8LF70), soybean (P13917), lupin (Q42369), wheat-1 (Q8H0K8), wheat-2 (Q53IQ4), and rye (Q6KE41). Conserved arginines are colored *orange*. *C*, comparison of structures between XEG-EDGP (*left panel*) and ANXI-TAXI-IA (*right panel*). Complexes are represented by *ribbon models*. *D*, putative model structure of an ANXI-EDGP (*left panel*) or XEG-TAXI-IA (*right panel*) complex.

imply that plants have evolved structures of GHIPs to inhibit specific GH families of enzymes that attack their cell walls. In addition to TAXI, wheat has xylanase inhibitor protein I, which possesses two independent enzyme-binding sites and is able to inhibit both GH10 and GH11 xylanases (31). Plants employ related proteins and mechanisms for target recognition of GH to protect their cell walls using conserved patterns of interacting residues.

Acknowlegments—We thank the beamline staff of SPring-8 and PF for data collection and Dr. H. Shiota, Yokohama City University, for supplying carrot callus, and Dr. J. R. H. Tame, Yokohama City University for English corrections.

REFERENCES

1. Henrissat, B. (1991) A classification of glycosyl hydrolases based on amino acid sequence similarities. *Biochem. J.* **280,** 309–316
2. Juge, N. (2006) Plant protein inhibitors of cell wall degrading enzymes. *Trends Plant Sci.* **11,** 359–367
3. Lagaert, S., Beliën, T., and Volckaert, G. (2009) Plant cell walls: protecting the barrier from degradation by microbial enzymes. *Semin. Cell Dev. Biol.* **20,** 1064–1073
4. Shang, C., Sassa, H., and Hirano, H. (2005) The role of glycosylation in the function of a 48-kDa glycoprotein from carrot. *Biochem. Biophys. Res. Commun.* **328,** 144–149
5. Pauly, M., Andersen, L. N., Kauppinen, S., Kofod, L. V., York, W. S., Albersheim, P., and Darvill, A. (1999) A xyloglucan-specific endo-β-1,4-glucanase from *Aspergillus aculeatus*: expression cloning in yeast, purification and characterization of the recombinant enzyme. *Glycobiology* **9,** 93–100
6. Hayashi, T. (1989) Xyloglucans in the primary cell wall. *Annu. Rev. Plant Physiol. Plant Mol. Biol.* **40,** 139–168
7. Qin, Q., Bergmann, C. W., Rose, J. K., Saladie, M., Kolli, V. S., Albersheim, P., Darvill, A. G., and York, W. S. (2003) Characterization of a tomato protein that inhibits a xyloglucan-specific endoglucanase. *Plant J.* **34,** 327–338
8. Naqvi, S. M., Harper, A., Carter, C., Ren, G., Guirgis, A., York, W. S., and Thornburg, R. W. (2005) Nectarin IV, a potent endoglucanase inhibitor secreted into the nectar of ornamental tobacco plants: isolation, cloning, and characterization. *Plant Physiol.* **139,** 1389–1400
9. Gebruers, K., Brijs, K., Courtin, C. M., Fierens, K., Goesaert, H., Rabijns, A., Raedschelders, G., Robben, J., Sansen, S., Sørensen, J. F., Van Campenhout, S., and Delcour, J. A. (2004) Properties of TAXI-type endoxylanase inhibitors. *Biochim. Biophys. Acta* **1696,** 213–221
10. Sansen, S., De Ranter, C. J., Gebruers, K., Brijs, K., Courtin, C. M., Delcour, J. A., and Rabijns, A. (2004) Structural basis for inhibition of *Aspergillus niger* xylanase by *Triticum aestivum* xylanase inhibitor-I. *J. Biol. Chem.* **279,** 36022–36028
11. Fierens, K., Gils, A., Sansen, S., Brijs, K., Courtin, C. M., Declerck, P. J., De Ranter, C. J., Gebruers, K., Rabijns, A., Robben, J., Campenhout, S., Volckaert, G., and Delcour, J. A. (2005) His^{374} of wheat endoxylanase inhibitor TAXI-I stabilizes complex formation with glycoside hydrolase family 11 endoxylanases. *FEBS J.* **272,** 5872–5882
12. Yoshizawa, T., Shimizu, T., Yamabe, M., Taichi, M., Nishiuchi, Y., Shichijo, N., Unzai, S., Hirano, H., Sato, M., and Hashimoto, H. (2011) Crystal structure of basic 7S globulin, a xyloglucan-specific endo-β-1,4-glucanase inhibitor protein-like protein from soybean lacking inhibitory activity against endo-β-glucanase. *FEBS J.* **278,** 1944–1954
13. Yoshizawa, T., Shimizu, T., Hirano, H., Sato, M., and Hashimoto, H. (2011) Purification, crystallization and x-ray diffraction study of extracellular dermal glycoprotein from carrot and the inhibition complex that it forms with an endo-β-glucanase from *Aspergillus aculeatus*. *Acta Crystallogr. Sect. F Struct. Biol. Cryst. Commun.* **67,** 830–832

14. Hoover, D. M., and Lubkowski, J. (2002) DNAWorks: an automated method for designing oligonucleotides for PCR-based gene synthesis. *Nucleic Acids Res.* **30,** e43
15. Lever, M. (1972) A new reaction for colorimetric determination of carbohydrates. *Anal. Biochem.* **47,** 273–279
16. Martinez-Fleites, C., Guerreiro, C. I., Baumann, M. J., Taylor, E. J., Prates, J. A., Ferreira, L. M., Fontes, C. M., Brumer, H., and Davies, G. J. (2006) Crystal structures of *Clostridium thermocellum* xyloglucanase, XGH74A, reveal the structural basis for xyloglucan recognition and degradation. *J. Biol. Chem.* **281,** 24922–24933
17. Miyatake, H., Hasegawa, T., and Yamano, A. (2006) New methods to prepare iodinated derivatives by vaporizing iodine labelling (VIL) and hydrogen peroxide VIL (HYPER-VIL). *Acta Crystallogr. D Biol. Crystallogr.* **62,** 280–289
18. Otwinowski, Z., and Minor, W. (1997) Processing of x-ray diffraction data collected in oscillation mode. *Methods Enzymol.* **276,** 307–326
19. Vagin, A., and Teplyakov, A. (1997) MOLREP: an automated program for molecular replacement. *J. Appl. Crystallogr.* **30,** 1022–1025
20. Terwilliger, T. (2004) SOLVE and RESOLVE: automated structure solution, density modification and model building. *J. Synchrotron Radiat.* **11,** 49–52
21. Emsley, P., and Cowtan, K. (2004) COOT: model-building tools for molecular graphics. *Acta Crystallogr. D Biol. Crystallogr.* **60,** 2126–2132
22. Brünger, A. T., Adams, P. D., Clore, G. M., DeLano, W. L., Gros, P., Grosse-Kunstleve, R. W., Jiang, J. S., Kuszewski, J., Nilges, M., Pannu, N. S., Read, R. J., Rice, L. M., Simonson, T., and Warren, G. L. (1998) Crystallography & NMR system: a new software suite for macromolecular structure determination. *Acta Crystallogr. D Biol. Crystallogr.* **54,** 905–921
23. Murshudov, G. N., Vagin, A. A., and Dodson, E. J. (1997) Refinement of macromolecular structures by the maximum-likelihood method. *Acta Crystallogr. D Biol. Crystallogr.* **53,** 240–255
24. Laskowski, R. A., MacArthur, M. W., Moss, D. S., Thornton, J. M. (1993) PROCHECK: a program to check the stereochemical quality of protein structure. *J. Appl. Crystallogr.* **26,** 283–291
25. Sandgren, M., Ståhlberg, J., and Mitchinson, C. (2005) Structural and biochemical studies of GH family 12 cellulases: improved thermal stability, and ligand complexes. *Prog. Biophys. Mol. Biol.* **89,** 246–291
26. Kanda, T., Wakabayashi, K., and Nisizawa, K. (1976) Synergistic action of two different types of endocellulase components from *Irpex lacteus* (*Polyporus tulipiferae*) in the hydrolysis of some insoluble celluloses. *J Biochem.* **79,** 997–1005
27. Gloster, T. M., Ibatullin, F. M., Macauley, K., Eklöf, J. M., Roberts, S., Turkenburg, J. P., Bjørnvad, M. E., Jørgensen, P. L., Danielsen, S., Johansen, K. S., Borchert, T. V., Wilson, K. S., Brumer, H., and Davies, G. J. (2007) Characterization and three-dimensional structures of two distinct bacterial xyloglucanases from families GH5 and GH12. *J. Biol. Chem.* **282,** 19177–19189
28. Shang, C., Shibahara, T., Hanada, K., Iwafune, Y., and Hirano, H. (2004) Mass spectrometric analysis of posttranslational modifications of a carrot extracellular glycoprotein. *Biochemistry* **43,** 6281–6292
29. Browner, M. F., Smith, W. W., and Castelhano, A. L. (1995) Matrilysin-inhibitor complexes: common themes among metalloproteases. *Biochemistry* **34,** 6602–6610
30. Törrönen, A., Harkki, A., and Rouvinen, J. (1994) Three-dimensional structure of endo-1,4-β-xylanase II from *Trichoderma reesei*: two conformational states in the active site. *EMBO J.* **13,** 2493–2501
31. Payan, F., Leone, P., Porciero, S., Furniss, C., Tahir, T., Williamson, G., Durand, A., Manzanares, P., Gilbert, H. J., Juge, N., and Roussel, A. (2004) The dual nature of the wheat xylanase protein inhibitor XIP-I: structural basis for the inhibition of family 10 and family 11 xylanases. *J. Biol. Chem.* **279,** 36029–36037

Cancer Biomarkers 10 (2011/2012) 175–183
DOI 10.3233/CBM-2012-0243
IOS Press

Use of quantitative shotgun proteomics to identify fibronectin 1 as a potential plasma biomarker for clear cell carcinoma of the kidney

Akira Yokomizo[a,*,1], Michiko Takakura[b,1], Yae Kanai[c], Tomohiro Sakuma[d], Junichi Matsubara[b], Kazufumi Honda[b], Seiji Naito[a], Tesshi Yamada[b] and Masaya Ono[b]
[a]*Department of Urology, Graduate School Medical Sciences, Kyushu University, Fukuoka, Japan*
[b]*Division of Chemotherapy and Clinical Research, National Cancer Center Research Institute, Tokyo, Japan*
[c]*Division of Molecular Pathology, National Cancer Center Research Institute, Tokyo, Japan*
[d]*BioBusiness Group, Mitsui Knowledge Industry, Tokyo, Japan*

Abstract. *Background*: Early detection would be one of the most effective means to improve the outcome of renal cell carcinoma (RCC). We searched for a new plasma marker for RCC using a label-free quantitative shotgun proteomics method.
Methods: Plasma proteins were digested by trypsin, and the resulting peptides were analyzed by 2-Dimensional Image Converted Analysis of Liquid chromatography mass spectrometry (2DICAL). An identified biomarker candidate was subjected to validation using the Amplified Luminescent Proximity Homogeneous Assay (AlphaLISA).
Results: Among a total of 23,407 independent MS peaks, we found that the mean intensity of 59 peaks significantly differed between 20 clear cell RCC patients and 20 healthy controls. MS/MS spectra from 16 of the 59 peaks matched the amino acid sequences of the fibronectin 1 (*FN1*) gene product. The increased plasma level of FN1 in RCC patients was validated in a cohort of in 77 patients and 130 healthy controls ($p < 0.0001$).
Conclusions: The FN1 is considered to be a promising biomarker candidate for clear cell RCC. Furthermore, AlphaLISA is an alternate to the conventional enzyme-linked immunosorbent assay and should prove useful for the rapid validation of biomarker candidates.

Keywords: Renal cell carcinoma, tumor marker, proteomics, fibronectin

1. Introduction

The incidence of renal cell carcinoma (RCC) has been increasing since 1980s in western countries as well as Japan and is now the third most common malignancy of the urinary tract following prostate and bladder cancers [1]. Although early detection and treatment are considered to be the most effective methods to improve the outcome of patients with any cancer, RCC patients often do not manifest clinical symptoms and receive medical attention until their tumors progress to advanced stages [2–4]. Recently, ultrasound and CT scan can detect smaller renal tumors. However, we do need an effective plasma biomarker for differentiating the malignant from the benign when a patient was found with a small renal mass, which cannot be easily judged from ultrasound or CT scan [5]. Therefore, it is necessary to identify the tumor marker better than neither ultrasound test nor CT scan in diagnosing small renal mass. If a sensitive but non-invasive blood assay that can detect early-stage RCC were available, it would greatly improve the curative rate of RCC.

Shotgun proteomics is an established technique in which whole proteins are enzymatically digested into a large array of small peptide fragments followed

*Corresponding author: Akira Yokomizo, Department of Urology, Graduate School of Medical Sciences, Kyushu University, 3-1-1 Maidashi, Higashi-ku, Fukuoka 812-8252, Japan. Tel.: +81 92 642 5603; Fax: +81 92 642 5618; E-mail: yokoa@uro.med.kyushu-u.ac.jp.
[1]These two authors contributed equally to this work.

ISSN 1574-0153/11/12/$27.50

by direct analysis by liquid chromatography and mass spectrometry (LC-MS). We previously developed software named 2DICAL that can provide a quantitative dimension to shotgun proteomics [6]. 2DICAL can accurately align different LC-MS data and compare the protein content of a theoretically unlimited number of samples without isotope labeling [7]. 2DICAL is highly advantageous methods in clinical studies that require the comparison of a statistically sufficient number of patient samples [8]. Using 2DICAL, we were able to identify diagnostic biomarkers for endometrial and pancreatic cancers [7,8] and predictive biomarkers for hematologic toxicities and therapeutic efficacy of gemcitabine treatment to patients with advanced pancreatic cancer [9].

In this study we compared the plasma proteome between RCC patients and healthy controls using 2DICAL with the aim to identify a new diagnostic biomarker that can be used for a blood test. RCC consists of clear cell (75%), papillary (10%), chromophobe (5%) and other subtypes [10], and we first focused on clear cell carcinoma, the most common subtype of RCC. We discovered a significant increase of circulating plasma FN1 in patients with RCC and confirmed its significance in a larger patient cohort using a newly established measurement system.

2. Materials and methods

2.1. Plasma samples

Plasma samples were prospectively collected from RCC patients, prostate cancer patients and healthy volunteers at the Department of Urology, Kyushu University Hospital (Fukuoka, Japan) between October 2000 and January 2008. To exclude sampling bias, all the patients' whole blood (7 ml) was collected in the same tube (EDTA-2Na tube, Venoject II, Terumo, Japan) before the surgery or first treatment. These blood samples were stored in 4°C for 1 hour and plasma was separated after centrifugation, aliquoted into 1 ml samples in 1.5 ml eppendorf tubes, and stored at −80°C. The control samples were collected and stored under the same condition. All the samples had the only one cycle of freeze-and-thaw. As we excluded the non-clear cell subtype and benign kidney tumors, the plasma from 77 histopathologically proven clear cell cancer patients were used for the analysis. Control plasma samples were randomly selected from 20 patients with prostate cancer and 130 healthy individuals after adjusting the age and gender. The clinical stage of each patient was classified according to the 7th edition UICC TNM classification [11]. Twenty RCC patients (excluding those in stage IV) were selected for analysis using 2DICAL in an effort to detect early stage biomarkers (Table 1).

2.2. Ethics

All individuals provided written informed consent authorizing the collection and use of their samples for research purposes. The protocol was reviewed and approved by the institutional ethics committee boards of the National Cancer Center Research Institute (Tokyo, Japan) and the Kyushu University (Fukuoka, Japan).

2.3. LC-MS

The 20 most abundant plasma proteins including albumin and immunoglobulin were removed using ProtPrep 20 Plasma Immunodepletion Kit (Sigma-Aldrich, St. Louis, MO) following the manufacturer's instructions. The depleted plasma samples were then digested with trypsin (Promega, Madison, WI) overnight at 37°C. The resulting peptides were randomized and measured in triplicate by LC-MS. LC separation in a linear gradient of 0 to 80% acetonitrile in 0.1% formic acid at a speed of 200 nL/minute for 60 minutes was conducted using a splitless nano-flow HPLC system (Hitachi High-technologies, Tokyo, Japan). MS data were acquired every second for 60 minutes by an electrospray ionization mass spectrometer (Q-TOF Ultima; Waters, Milford, MC) directly linked to an LC in the range of 250–1600 m/z. MS peaks were detected, normalized, and quantified using the in-house 2DICAL software package as described previously [7]. A serial ID number was applied to each of the MS peaks detected (ID 1 to 23,407) [9]. The stability of LC-MS was monitored by calculating the correlation coefficient (CC) and coefficient of variance (CV) values among triplicate measurements.

2.4. Protein identification by tandem mass spectrometry (MS/MS)

Peak lists were generated using the Mass Navigator software package (version 1.2) (Mitsui Knowledge Industry, Tokyo, Japan) and searched against the SwissProt database (SwissProt_57.6.fast) using the Mascot software package (version 2.2.06) (Matrix Science, London, UK). The search parameters used were as follows: A database of human proteins was selected.

Table 1
Clinicopathological characteristics of individuals examined in this study

		Cases anlyzed by AlphaLISA (n = 227)			Cases analyzed by 2DICAL (n = 60)	
		RCC (n = 77)	PCa (n = 20)	Healthy (n = 130)	RCC (n = 20)	Healthy (n = 20)
Age	(mean ± SD)	61.2 ± 11.0	64.8 ± 6.9	65.4 ± 10.5	63.8 ± 8.5	66.0 ± 7.9
Gender						
	Male	57	20	113	20	20
	Female	20		17	0	0
Clinical stage*						
	I	56	9		17	
	II	3	11		2	
	III	3			1	
	IV	9			0	
	Unknown	6				
Tumor side						
	Right	38			11	
	Left	39			9	
Histologic type						
	Clear cell	77			20	
	Chromophobe	0			0	
	Papillary	0			0	
	Unclassified	0			0	

*according to TNM Classification of Malignantu Tumors (International Union Against Cancer), 7th Edition
RCC, renal cell carcinome; PCa, prostate cancer; AlphaLISA, amplified luminescence proximity homogeneous assay; 2DICAL, two-dimensional image convert

Trypsin was designated as the enzyme, and up to one missed cleavage was allowed. Mass tolerances for precursor and fragment ions were ± 0.2 Da and ± 0.8 Da, respectively. The score threshold was set to the value over 20 for peptide search. If a peptide matched to multiple proteins, the protein name with the highest Mascot score was selected.

2.5. *Western blot analysis*

Plasma samples were fractionated with SDS-PAGE and electroblotted onto a polyvinylidene difluoride membrane (Millipore, Billerica, MA), as described previously [9,12]. Primary antibodies used were mouse monoclonal anti-FN1 antibody (R&D Systems, Minneapolis, MN) and mouse monoclonal antibody against human complement C3b-α (PROGEN, Heidelberg, Germany) [8]. The membrane was then incubated with the primary antibody and subsequently with the relevant horseradish peroxidase-conjugated anti-mouse IgG as described previously. Blots were developed using an enhanced chemiluminescence (ECL plus) detection system (GE Healthcare, Buckinghamshire, UK).

2.6. *AlphaLISA*

An assay for measuring soluble FN1 was constructed using the AlphaLISA system (PerkinElmer, MA) which is a bead-bead nonradioactive technology. In brief, when a biological interaction brings the beads into close proximity, a cascade of chemical reactions is induced resulting in a greatly amplified signal, then a photosensitizer present in the beads converts ambient oxygen to a more excited singlet state upon laser excitation. Biotinylated rabbit polyclonal anti-FN1 antibody and mouse polyclonal anti-FN1 antibody were purchased from Abcam (Cambridge, UK). The AlphaLISA procedure was carried out according to the protocol provided by the manufacturer.

2.7. *Statistical methods*

The Mann-Whitney U-test was employed for statistical analysis of the correlation between RCC patients and controls as well as the plasma values of FN1 and clinicopathological parameters. Welch's t-test was employed for 2DICAL analysis. Kaplan–Meier analysis was used to examine the correlation of the plasma value of FN1, cancer-specific survival and overall survival. The area under the curve (AUC) of the receiver operating characteristic (ROC) was calculated to evaluate its diagnostic significance.

3. Results

3.1. *Identification of plasma proteins significantly increased in RCC patients*

Plasma proteins of 20 patients with RCC and 20 healthy individuals were digested by trypsin, and

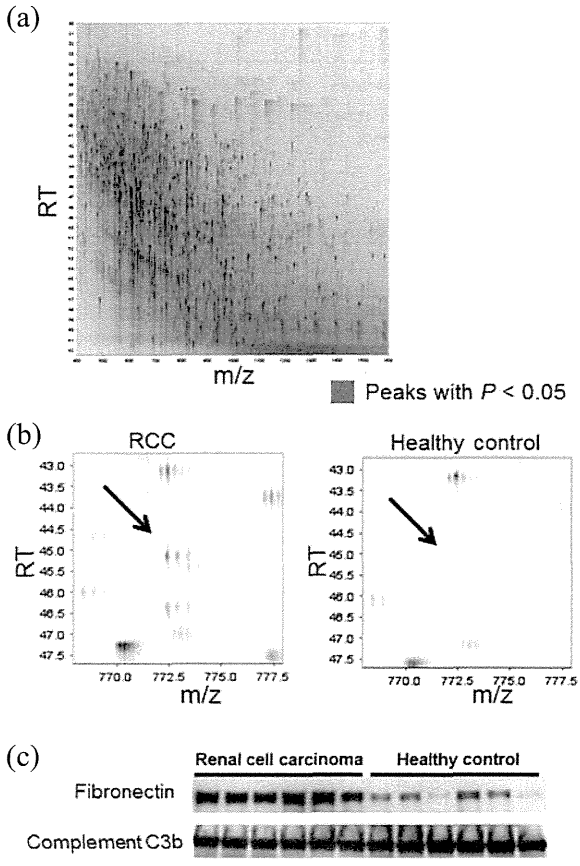

Fig. 1. (a) Two-dimensional display of all the MS peaks in 2DICAL. The 59 MS peaks whose mean intensity significantly differed in renal cell carcinoma patients from healthy controls ($p < 0.05$, Welch's t-test) are highlighted in red. (b) Two representative MS peaks with the smallest p-value. RT; retention time. (c) Detection of plasma FN1 and complement C3b-α (loading control) by immunoblotting.

the resulting peptides were subjected to LC-MS. A total of 23,407 MS peaks per sample were detected in the range of 250–1,600 m/z and 25–65 minutes across the 40 plasma samples, and their relative mass intensity was calculated using 2DICAL. The mean CC and CV values of the 23,407 MS peaks were over 0.95 and under 0.15, respectively, confirming the high reproducibility of LC-MS. Among the 23,407 MS peaks we found that the mean intensity of 59 peaks (in triplicate) significantly differed between 20 RCC patients and 20 healthy controls ($p < 0.05$, Welch's t-test). Thirty six peaks were increased and 23 peaks were decreased in RCC patients and the statistical significance was confirmed by calculating the false discovery rate (FDR) values [13] (data not shown). Figure 1a shows a representative 2-dimensional view in which all the ~23,000 MS peaks were displayed with the m/z along the X axis and the RT of LC along the Y axis and the 59 MS peaks are highlighted in red. Figure 1b shows a representative MS peak that increased in the plasma of RCC patients.

3.2. Protein identification by MS/MS

Fifty seven MS/MS spectra acquired from the 59 MS peaks matched to 21 peptide sequences deposited in the human protein database (Table 2). Remarkably, 16 of the 21 peptides were found to be derived from the amino acid sequence of *FN1* gene product (Supportive information Figs S1 and S2). The identification and differential expression of FN1 protein were confirmed by immunoblotting (Fig. 1c).

3.3. Verification by AlphaLISA

To validate the increased level of plasma FN1, we constructed a new assay that can quantify the amount of FN1. The AlphaLISA showed high reproducibility with a median CV value of 0.08 among triplicates and linearity in the range of 50–800 μg/ml.

The plasma concentration of FN1 was measured in 77 RCC patients, 20 prostate cancer (PCa) patients, and 130 healthy individuals by AlphaLISA. There was a significant difference between RCC patients (405 $\pm$ 153 μg/ml) and healthy individuals (294 $\pm$ 102 μg/ml) with a p-value of 1.8×10^{-7} (Mann-Whitney U test) (Fig. 2a). The plasma concentration of FN1 was not elevated in PCa patients (306 $\pm$ 81 μg/ml). The AUC value of ROC for plasma FN1 concentration of RCC patients to healthy individuals was calculated to be 0.71 for all stages, stage I and II and stage III and IV (Fig. 2b). *The optimum diagnostic cut-off point of FN1 was identified at 377 μg/ml by the AUC curve. At this point, sensitivity, specificity, PPV and NPV were 53%, 82%, 64% and 75% respectively. And the fibronectin concentration in each clinical stage was shown in Fig. 2c.*

3.4. Correlation of plasma concentration of FN1 and clinicopathological parameters

The statistical analyses were performed to *detect* the correlation of plasma concentration of FN1 and clinical stage (Fig. 2c), but there were no significant differences. Also, there were no significant correlations between concentration of FN1 and the other clinicopathological parameters, such as tumor size, tumor grade and vascular involvement (data not shown). Furthermore, Kaplan–Meier analysis, used to analyze the correlation

Table 2
Summary of protein identification by tandem mass spectrometry

ID	m/z	RT	Charge	Control (mean ± SD)	RCC (mean ± SD)	P Values**	Mascot Score	Peptide sequence	Protein description
2411	799.3815	36.479	3	15±6	25±13	5.09E-03	84.46	RPGGEPSPEGTTGQSYNQYSQR	Fibronectin
3454	622.3328	39.679	3	14±4	20±8	8.59E-03	75.78	HTSVQTTSSGSGPFTDVR	Fibronectin
3948	647.3662	49.283	2	13±2	17±7	9.54E-03	54.92	DLQFVEVTDVK	Fibronectin
2039	978.5337	47.716	2	16±7	30±20	6.08E-03	53.45	EESPLLIGQQSTVSDVPR	Fibronectin
750	706.3586	44.432	2	101±45	73±28	2.34E-02	51.41	KWQEEMELYR	Apolipoprotein A-I
2614	815.4614	46.26	2	11±4	18±12	1.61E-02	50.73	VDVIPVNLPGEHGQR	Fibronectin
2068	646.379	52.817	2	17±7	26±15	1.96E-02	46.43	GATYNIIVEALK	Fibronectin
2854	997.5346	53.967	2	18±5	23±11	4.61E-02	41.28	NTFAEVTGLSPGVTYYFK	Fibronectin
1231	675.3681	45.847	2	28±11	52±34	4.38E-03	40.93	WLPSSSPVTGYR	Fibronectin
1816	772.8941	45.207	2	17±7	32±20	5.88E-03	35.57	SYTITGLQPGTDYK	Fibronectin
2439	638.3344	38.15	2	22±7	30±13	1.54E-02	32.64	HVVPNEVVVQR	Gelsolin
2569	555.8103	40.153	2	16±5	25±13	6.00E-03	32.26	STTPDITGYR	Fibronectin
1155	772.419	45.123	2	43±14	64±34	1.27E-02	31.79	SYTITGLQPGTDYK	Fibronectin
2771	701.8697	39.773	2	13±5	22±13	6.58E-03	30.7	HYQINQQWER	Fibronectin
2611	592.8548	43.895	2	26±11	19±6	1.87E-02	30.31	IQNILTEEPK	Serum paraoxonase
1371	511.785	35.131	2	44±12	55±17	1.82E-02	29.99	ATVVYQGER	Beta-2-glycoprotein 1
1826	867.5129	50.364	2	20±7	36±22	3.48E-03	29.17	NLQPASEYTVSLVAIK	Fibronectin
1813	701.366	39.859	2	28±7	42±18	4.02E-03	27.25	HYQINQQWER	Fibronectin
2417	576.8117	42.453	2	16±5	26±15	5.75E-03	26.67	FTNIGPDTMR	Fibronectin
1794	964.0527	58.428	2	23±8	34±20	2.61E-02	23.59	VTWAPPPSIDLTNFLVR	Fibronectin
1377	629.36	53.672	2	39±23	24±9	7.97E-03	21.25	DLAVVDAKDAIK	EXOC1_HUMAN

RT, retention time; RCC, renal cell carcinoma
**Welch's t-test.

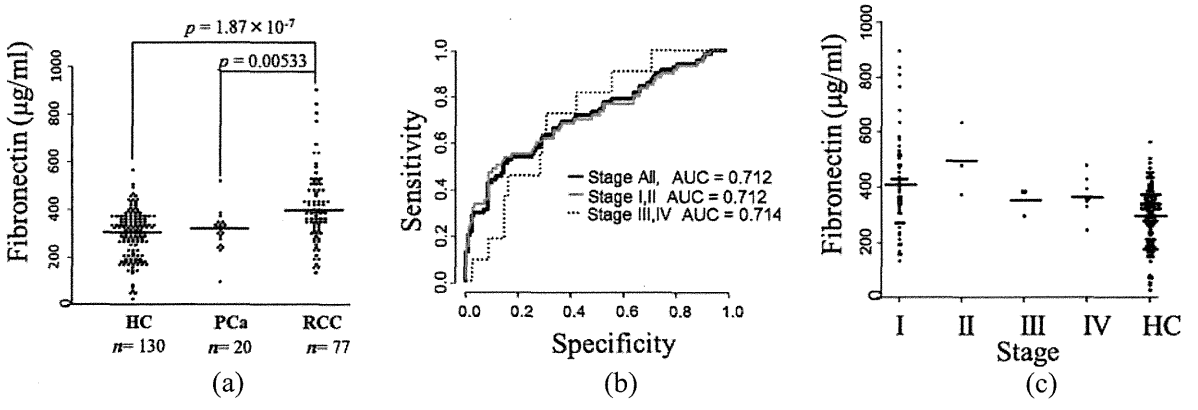

Fig. 2. (a) Concentration of plasma FN1 in each group. The FN1 concentration of renal cell carcinoma patients ($n = 77$), healthy individuals ($n = 130$) and prostate cancer patients ($n = 20$) was measured by AlphaLISA. There were significant differences in renal cell carcinoma patients compared to healthy individuals and prostate cancer patients, but not between healthy individuals and prostate cancer patients (Mann-Whitney U test). Horizontal lines represent the average concentration. (b) Receiver operating characteristic (ROC) curve for plasma FN1 concentration. AUC value of ROC for plasma FN1 concentration of RCC patients to healthy individuals was calculated to be 0.71 for all stages, stage I and II and stage III and IV. Similar AUC value of earlier stage to advanced stage suggested the possibility of early detection of renal cell carcinoma by plasma FN1. (c) The plasma FN1 concentration in each clinical stage. HC; healthy control.

of serum value of FN1, cancer-specific survival and overall survival, failed to prove any statistical significant differences with a median follow up of 47.6 months after surgery (data not shown).

4. Discussion

FN1 is a high-molecular-weight extracellular matrix protein that plays an important role in cellular attachment and cell spread [14,15]. FN1 can be soluble or insoluble, is produced by hepatocytes and various cell types and is bound to integrins [16]. Altered expression of FN1 is known to change the morphology of several tumor cell lines [17]. In several studies of different RCC cell lines, FN1 was shown to be secreted into the culture medium and suggested to influence the movement and invasion of these cells [18–20]. Another study showed FN1 plasma levels signif-

icantly elevated in localized and metastatic RCC patients compared to a control group [21]. According to "THE HUMAN PROTEIN ATLAS" (http://www.proteinatlas.org/ENSG00000115414), FN1 is expressed *in* extracellular matrix and stromal cell. FN1 is expressed weakly in normal kidney and relatively higher expressed in kidney cancer. It could be considerable that higher plasma levels of FN1 is secreted from these extracellular matrix and stromal cell in kidney cancer. A recent study suggested that FN1 mRNA expression was higher in RCC compared to normal renal tissue and correlated with advanced disease, suggesting that FN1 mRNA expression might serve as a marker for RCC aggressiveness [22]. Although the researchers failed to measure the plasma concentration of FN1, this study supports the results described herein obtained by proteome based screening.

The results of plasma FN1 from 2DICAL analysis were validated in a hundreds-scale cohort using a different methodology. AlphaLISA confirmed that the plasma level of FN1 was up-regulated in the early stage of RCC, which suggested that the FN1 plasma levels might be a tool for screening and diagnosis of RCC. However, there a limitation to introduce FN1 for screening of RCC, because plasma concentrations between patients and controls were overlapped extensively, and FN1 was not examined in benign renal tumors.

RCC comprises five histologically distinct subtypes classified by morphologic and pathologic features including clear cell (75%), papillary (10–15%), chromophobe (5–10%), collecting duct, and unclassified subtypes. We have previously reported that each RCC subtype has a totally different genetic profile by whole genome SNP array [10]. Therefore, each subtype should have a specific biomarker. In this study, we focused on clear cell RCC because it is the most abundant subtype of RCC and hence should be a first target of screening. Our comprehensive study of proteomics led to the possibility that monitoring the level of plasma FN1 could be clinically useful for the screening and diagnosis of RCC patients. The most of the *patients* we analyze were clinical stage I (56 cases / total 77 cases), and they had no symptoms such as febrile and *showed* normal range of C-reactive protein. Therefore, we believe that FN1 was not derived from acute phase reaction. Reports of the elevation of the plasma level of FN1 in RCC exist in the literature [21], but its clinical usage has not yet been described. One of the reasons may be the lack of applicable clinical test such as ELISA for FN1. The assessment of plasma FN1 levels must be determined for a large scale clinical cohort, but the construction of an easy clinical test such as ELISA will be needed for its completion.

Acknowledgments

We thank Ms. Ayako Igarashi, Ms. Tomoko Umaki, and Ms. Yuka Nakamura for their technical assistance.

Disclosure of potential conflicts of interest

These sponsors had no role in the design of the study, the collection of the data, the analysis and interpretation of the data, the decision to submit the manuscript for publication, or the writing of the manuscript.

Grant supports

Funding was received from the Program for Promotion of Fundamental Studies in Health Sciences conducted by the National Institute of Biomedical Innovation of Japan, and the Third-Term Comprehensive Control Research for Cancer and Research on Biological Markers for New Drug Development conducted by the Ministry of Health, Labour and Welfare of Japan.

Conflicts of interest

None.

References

[1] S.H. Landis, T. Murray, S. Bolden, P.A. Wingo. Cancer statistics, 1999, CA Cancer J Clin 49 (1999), 8-31.

[2] A.J. Schrader, Z. Varga, A. Hegele, S. Pfoertner, P. Olbert, R. Hofmann. Second-line strategies for metastatic renal cell carcinoma: classics and novel approaches, J Cancer Res Clin Oncol 132 (2006), 137-149.

[3] B.I. Rini, S. Halabi, R. Barrier, K.A. Margolin, D. Avigan, T. Logan et al. Adoptive immunotherapy by allogeneic stem cell transplantation for metastatic renal cell carcinoma: a CALGB intergroup phase II study, Biol Blood Marrow Transplant 12 (2006), 778-785.

[4] C. Gouttefangeas, A. Stenzl, S. Stevanovic, H.G. Rammensee. Immunotherapy of renal cell carcinoma, Cancer Immunol Immunother 56 (2007), 117-128.

[5] M. Remzi, M. Marberger. Renal tumor biopsies for evaluation of small renal tumors: why, in whom, and how? Eur Urol 55 (2009), 359-367.

[6] M. Ono, M. Shitashige, K. Honda, T. Isobe, H. Kuwabara, H. Matsuzuki et al. Label-free quantitative proteomics using large peptide data sets generated by nanoflow liquid chromatography and mass spectrometry, Mol Cell Proteomics 5 (2006), 1338-1347.